Control Engineering Practice 59 (2017) 111–126

Contents lists available at ScienceDirect

Control Engineering Practice

journal homepage: www.elsevier.com/locate/conengprac

Series Active Variable Geometry Suspension application to comfort enhancement☆

Carlos Arana[a,b], Simos A. Evangelou[a,*], Daniele Dini[b]

[a] Department of Electrical and Electronic Engineering, Imperial College London, UK
[b] Department of Mechanical Engineering, Imperial College London, UK

ARTICLE INFO

Keywords:
Vehicles
Vibration control
Mechatronics

ABSTRACT

This paper explores the potential of the Series Active Variable Geometry Suspension (SAVGS) for comfort and road holding enhancement. The SAVGS concept introduces significant nonlinearities associated with the rotation of the mechanical link that connects the chassis to the spring-damper unit. Although conventional linearization procedures implemented in multi-body software packages can deal with this configuration, they produce linear models of reduced applicability. To overcome this limitation, an alternative linearization approach based on energy conservation principles is proposed and successfully applied to one corner of the car, thus enabling the use of linear robust control techniques. An $\mathcal{H}_\infty$ controller is synthesized for this simplified quarter-car linear model and tuned based on the singular value decomposition of the system's transfer matrix. The proposed control is thoroughly tested with one-corner and full-vehicle nonlinear multi-body models. In the SAVGS setup, the actuator appears in series with the passive spring-damper and therefore it would typically be categorized as a low bandwidth or slow active suspension. However, results presented in this paper for an SAVGS-retrofitted Grand Tourer show that this technology has the potential to also improve the high frequency suspension functions such as comfort and road holding.

1. Introduction

According to MarketsandMarkets, the automotive suspension market will be worth $ 66.2bn by 2018, and most of the premium/luxury vehicles will be equipped with active or semi-active suspensions. New technological solutions, particularly electromechanical, that help bridge the gap between the performance of high bandwidth active suspensions and the simplicity, robustness and low cost of passive suspensions, seem to have an important role to play in the coming decades.

Much research in road vehicle suspensions has already taken place into reducing the conflict between achieving simultaneously passenger comfort and road holding (Sammier, Sename, & Dugard, 2003). In broad terms, depending on the suspension force unit nature, three main suspension types can be distinguished: passive, semi-active and active (Sharp & Crolla, 1987). It is widely accepted that compared to passive and semi-active suspensions active suspension offers the best performance in relation to comfort and road holding (Sharp & Peng, 2011; Tseng & Hrovat, 2015). However, in spite of their advanced capabilities, active suspensions have had a limited impact in the automotive market because of various disadvantages, related to weight, size, power requirements and complexity.

The Series Active Variable Geometry Suspension (SAVGS) (Evangelou et al., 2011), recently introduced in Arana, Evangelou and Dini (2015), aims to provide better performance than passive and semi-active suspensions while avoiding the main active suspension disadvantages. It is a purely electromechanical solution that relies on well known, widely available technology such as rotary electric motors and epicyclic gearboxes. It combines the classical variable geometry suspension concept (Sharp, 1998), in which actuation forces are applied perpendicularly to the main suspension forces in order to reduce energy expenditure, with features of more conventional active suspensions in which a direct contribution to the main suspension forces is made. Some key advantages of the SAVGS are its fail safe operation in case of power loss and/or actuator blockage, and its *active on demand* capability, with potentially zero power consumption when idling. In its simplest embodiment, shown in Fig. 1, a single mechanical link (SL) is introduced between the chassis and the upper end of the conventional spring-damper (SD) unit. By controlling the rotation of the SL, the elongation and orientation of the SD can be altered and the

☆ This work was supported by the UK Engineering and Physical Sciences Research Council and by Imperial Innovations. Data supporting this publication can be obtained on request from cap-publications@imperial.ac.uk.

* Corresponding author.
E-mail addresses: carlos.arana-remirez10@imperial.ac.uk (C. Arana), s.evangelou@imperial.ac.uk (S.A. Evangelou), d.dini@imperial.ac.uk (D. Dini).

http://dx.doi.org/10.1016/j.conengprac.2016.11.011
Received 15 May 2016; Received in revised form 17 November 2016; Accepted 18 November 2016
Available online 01 December 2016

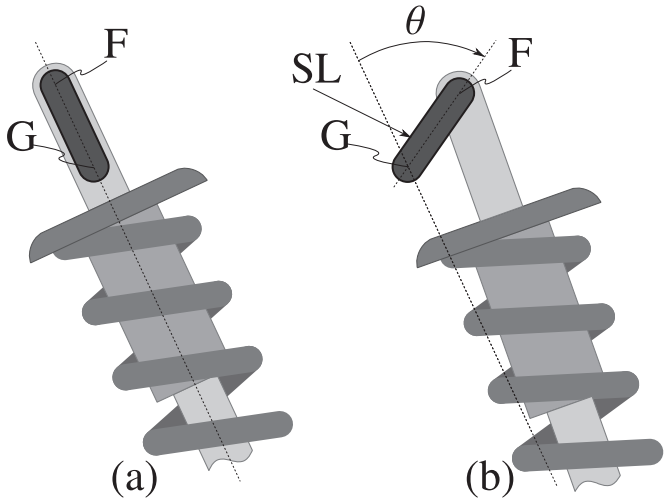

Fig. 1. Single-link variant of the SAVGS concept. The mechanical link, SL, connects point G in the chassis to point F in the upper end eye of the SD through pin joints. When no actuation torque is applied between the chassis and the SL, the system remains in equilibrium in position (a). Alternative configurations, such as (b), can be reached by applying a torque about point G.

suspension response can be enhanced.

The application of this technology to low frequency suspension functions such as pitch attitude control (Arana et al., 2015, 2012), and control of combined (roll and pitch) chassis attitude motions and vehicle directional response (Arana, Evangelou, & Dini, 2014, 2016) under longitudinal and lateral acceleration, using PID based controllers, has already been investigated with promising results reported. The control of the SAVGS in the context of high frequency suspension functions (i.e. comfort and road holding enhancement) has been investigated in Cheng, Evangelou, Arana, and Dini (2015) by a linear $\mathcal{H}_\infty$ scheme to control a nonlinear quarter car model with a double-wishbone suspension arrangement. Various methods for the high frequency control of active suspensions in general have been proposed in the literature, ranging from $\mathcal{H}_\infty$, Model Predictive, Sliding Mode, Backstepping, Fuzzy Logic, and Neural Network control (Basari, Sam, & Hamzah, 2007; Cao, Liu, Li, & Brown, 2008; Chen & Huang, 2006; Chen & Scherer, 2004; Gaspar, Szaszi, & Bokor, 2003; Li, Yu, Hilton, & Liu, 2013; Sammier et al., 2003; van der Sande et al., 2013; Zin, Sename, Gaspar, Dugard & Bokor, 2008) typically utilizing quarter-car models and in some cases linear half-car or full-car models. The SAVGS in the current embodiment involves a rotating link that introduces a geometric nonlinearity whose control is difficult to synthesize with conventional car models.

This paper provides a comprehensive study of the SAVGS and its control in the context of high frequency suspension functions, in a linear $\mathcal{H}_\infty$ control framework but which includes a methodology to account appropriately for the significant plant nonlinearity. This framework facilitates the synthesis of SAVGS control that can exploit optimally the full actuator range and that is effective in relation to passenger comfort and road holding. Thus the work significantly advances previous work (Cheng et al., 2015) and provides a number of new contributions, including: 1) an energy-based methodology for the derivation of simple linear quarter-car models of series active suspensions with lumped geometric nonlinearity, that are accurate for a wide range of operating conditions (Section 2), as opposed to linearized models that are only accurate about a single trim condition; 2) the synthesis of an $\mathcal{H}_\infty$ controller for the SAVGS, effectively tuned for comfort and road holding enhancement by looking at the singular values and singular directions of the system (Section 3), rather than tuned exclusively by iteration based on control bandwidth and simulation results; 3) the introduction of exogenous disturbances into the $\mathcal{H}_\infty$ synthesis framework, beyond road disturbances, to control motions related to load transfer arising from longitudinal and/or lateral vehicle accelerations, and to provide suspension deflection tracking capability at low frequencies for future integration of low and high frequency suspension controls (Section 3); 4) the introduction into the $\mathcal{H}_\infty$ synthesis framework of additional measurement signals based on the expected availability of sensors, and of an account of the dynamics of the actuator and its (inner) position control loops (Section 3); and 5) the assessment of the SAVGS performance and of the quality of the proposed control, in comparison to passive suspension, when the vehicle is subjected to a wide range of standard disturbances by virtually testing its operation through simulation with nonlinear, multi-body, quarter-car and full-car models (Section 4). The study in the paper focusses on a Grand Tourer (GT) with vehicle and SAVGS parameters as provided in the Appendix.

The conclusions drawn from this work are summarized in Section 5.

2. Modeling and linearization of a quarter of a car retrofitted with the SAVGS

Although nonlinear multi-body models of the vehicle and its suspension are appropriate for virtually testing the SAVGS, they are not the best representation of the system for control synthesis. Linear models, on the other hand, enable the application of a wider range of control techniques and facilitate the study of the system dynamics in the frequency domain.

This section introduces the nonlinear SAVGS-retrofitted vehicle suspension model and proposes an efficient, effective, hand-derived linearization procedure for it based on energy conservation principles. This linearization procedure is described in Section 2.3, but first the scene is set up to highlight the limitations of the conventional linearization approach for the problem at hand. Conventional linearization results in models that are accurate only for *small* perturbations of the states and inputs from a given trim point, as opposed to the accurate behaviour achieved for large perturbations in some of the states with the model that will be described in Section 2.3.

Therefore, the reference nonlinear models that will serve as benchmark for different linearization procedures are first presented in Section 2.1. These nonlinear quarter-car models, which are built with a multi-body building software (Autosim (Anon, 1998)), will also be used in subsequent sections to test the proposed control system and to evaluate the performance of the SAVGS. Secondly, Section 2.2 analyzes the conventional linearization procedure and assesses its limitations for the problem at hand. Lastly, an energy-based linearization procedure is proposed in Section 2.3. The use of the resulting model in subsequent sections is justified based on the reduced model size and on the greatly increased range of operating conditions for which a single linear model is applicable, due to the cancellation of the geometric nonlinearity introduced by the SL.

2.1. Reference nonlinear models

Nonlinear multi-body quarter-car models of the passive and SAVGS-retrofitted suspensions have been defined in AutoSim based on the double-wishbone geometric arrangement shown in Fig. 2. In the passive case the nonlinear model comprises a sprung mass (chassis), an unsprung mass (wheel+tire), two massless wishbones (upper and lower), a conventional spring/damper, and a road tire compression force proportional to the tire deflection and tire deflection rate – this acts on the unsprung mass to support the overall mass of the quarter car and to introduce road forcing. In the SAVGS case the nonlinear quarter-car model additionally includes the new mechanical link, SL, and the actuator 'input'. Depending on how the quarter-car model is used (this will become apparent from subsequent discussions), the actuator input is either: (a) a torque on the SL generated by an also included dynamic model of the actuator that is operated by an inner position control loop as described in Arana et al. (2015), or (b) the

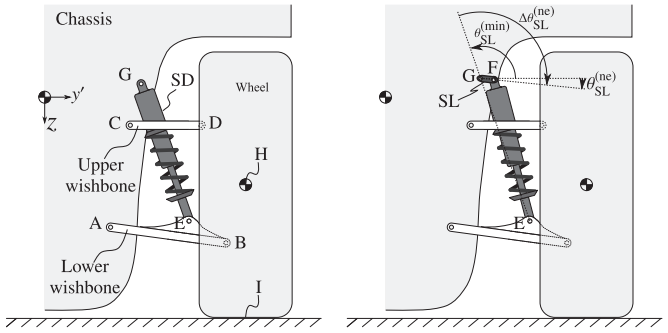

Fig. 2. Passive (left) and SAVGS-retrofitted (right) double-wishbone suspension in the nominal equilibrium configuration.

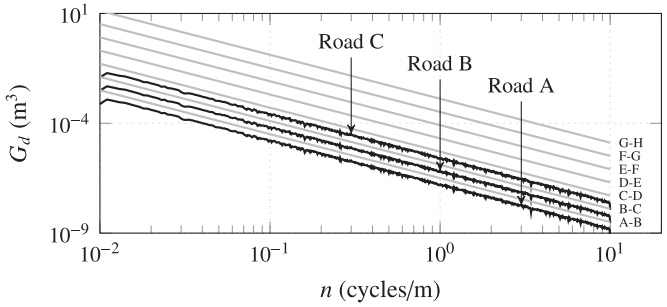

Fig. 3. Random road characteristics: displacement power spectral density, G_d, as a function of spatial frequency n. Boundaries between road classes A to H as defined in ISO (1995) are shown in gray. PSDs for roads profiles A to C considered in this work are shown in black and correspond to good, average and poor quality roads.

angle or angular speed of the SL with the actuator dynamics neglected. The nonlinearities considered in these models arise from the nonlinear force vs. speed characteristic of the damper as well as from the kinematics of the mechanical chain formed by the chassis, lower wishbone, wheel and upper wishbone. Suspension stroke limits have not been modeled. In the SAVGS case, additional nonlinearities appear due to the rotation of the SL and to the nonlinear dynamics and control of the SAVGS actuator (see (Arana et al., 2015) for more details on this).

The right-handed $x'y'z$ reference frame is attached to the chassis with the z axis pointing downwards and the y' axis parallel to the ground and pointing towards the wheel. Angles, such as SL or wishbone angles, are measured around the x' axis taking the orientation of the y' axis as zero angle. For any given suspension configuration, $\theta_{SL}^{(min)}$ refers to the SL angle that would lead to the maximum SD extension. Conversely, $\theta_{SL}^{(min)} + \pi$ would lead to the maximum SD compression. Superscript$^{(ne)}$ denotes *nominal equilibrium* and refers to some reference equilibrium configuration.

2.1.1. Omission of lateral tire forces

In most suspension studies that focus on comfort and road holding, the vehicle is assumed to be moving in a straight line and at a constant forward speed over an uneven road. Under these conditions, lateral tire forces are typically neglected to reduce model complexity. However, and depending on the suspension geometry, the wheel may undergo significant lateral and rotational motions as it moves vertically with respect to the sprung mass. These, in turn, lead to changes in camber and non-zero sideslip angles that can produce significant variations in lateral tire forces that affect the vertical dynamics of the system. The interested reader is referred to Fergani, Sename, and Dugard (2016), Gáspár & Németh for a recent and more in-depth treatment of the coupling between vertical and lateral dynamics.

Here, the effect of the lateral tire forces has been analyzed by simulating the passive nonlinear multi-body quarter-car model (arrangement shown on the left in Fig. 2) with rear axle parameter values, with and without lateral tire forces (produced by a standard sideslip model (Sharp & Bettella, 2003; Sharp, 2004)), over three typical random road profiles (A to C in Fig. 3) at a fixed forward speed of 100 km/h. The power spectral densities (PSD) of vertical sprung mass acceleration (related to comfort), dynamic suspension deflection (relevant to identify suspension travel requirements) and dynamic tire deflection (related to road holding), have been obtained with and without lateral tire forces. Discrepancies between the PSDs due to the lateral tire forces depend on the level of road disturbance as well as on the vehicle forward speed. They are 1) greater for rougher roads as this implies larger lateral wheel motions and camber changes and therefore larger lateral tire forces; and 2) smaller for larger forward vehicle speeds as the sideslip angle resulting from any given rate of lateral motion decreases with forward speed. For the vehicle and operating conditions considered in this work, the maximum difference occurs in the PSD of dynamic tire deflection and reaches 1.2 dB/Hz at ~5 Hz for road C. Thus, although it may not be appropriate to state that lateral tire forces are negligible in general, it is reasonable to omit them for the suspension geometry and disturbance levels considered here.

2.2. Conventional linearization of the multi-body model

Modeling of the kinematics and dynamics of a multibody system results in nonlinear equations of motion that can be linearized about any trim point, using standard theory, either by hand or automatically with the help of software. Autosim has the capability to perform such standard linearizations symbolically and provide the linearized equations of motion in state-space form, for any multibody model derived with it. The resulting equations are valid for any trim point and the corresponding equilibrium states and inputs can be found by nonlinear simulation and used to evaluate numerically the state-space matrices. As the nonlinear model of the SAVGS-retrofitted quarter-car has already been defined in Autosim, the linear model used in this section has also been derived with Autosim.

2.2.1. Selection of damping coefficient

Although the conventionally linearized models are accurate for *small* perturbations from any given trim point, significant discrepancies with respect to the nonlinear models may arise for realistic disturbance levels. This problem becomes particularly acute if the characteristics of the nonlinear suspension damper, which displays a piecewise response with different damping coefficients for bump and rebound as well as for low and high extension/compression rates, are linearized incorrectly. By comparing the PSDs obtained with the linear and nonlinear models for the same road profiles as previously discussed (and shown in Fig. 3), a linear damping coefficient that captures the dynamics of the system reasonably well for the range of excitations of interest has been estimated. In particular, the linear damping coefficient that minimizes the (equally weighted) sum of the square of the errors between the linear and nonlinear PSDs of sprung mass acceleration, dynamic suspension deflection and dynamic tire deflection, for roads A to C and for the range of frequencies of interest has been found; a grid of 200 logarithmically spaced frequencies has been considered in the 0.3–50 Hz range. This linear damping coefficient, which is 9940 Ns/m or approximately 40% of that displayed by the real damper at low compression speeds (24240 Ns/m), is used in the linear models in subsequent sections.

2.2.2. Frequency response

This section analyzes the Bode magnitude responses of the rear suspension of the GT and assesses the quality of the predictions obtained with the conventionally linearized model when the system is operated far from the trim state for which the model was linearized. For this assessment, three inputs are considered: rate of change of road height, external load acting vertically on the sprung mass (to represent

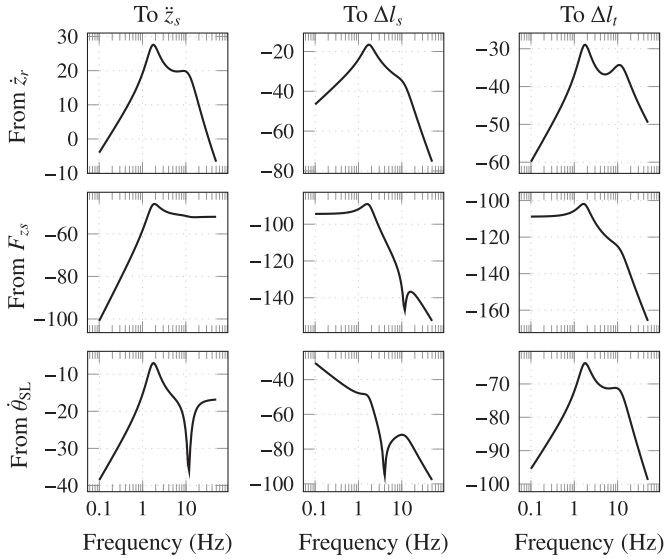

Fig. 4. Gains (in dB) from vertical road speed (top), external vertical force acting on the sprung mass (middle) and SL angular speed (bottom) to sprung mass acceleration (left), dynamic suspension deflection (center) and dynamic tire deflection (right) for the rear suspension of the GT. Results correspond to the nominal SL angle offset $\Delta\theta_{SL}^{(ne)}$.

longitudinal and lateral load transfers due to horizontal vehicle accelerations) and angular speed of the SL (the control action). The outputs considered are the ones typically reported in the literature: sprung mass acceleration (comfort), dynamic suspension deflection (suspension travel requirements) and dynamic tire deflection (road holding).

The Bode magnitude responses for $\theta_{SL} = \theta_{SL}^{(ne)} = \theta_{SL}^{(min)} + 90$ deg are shown in Fig. 4 for the rear suspension of the GT. With the damping coefficient found in Section 2.2.1, the GT displays the typical double-hump response to road irregularities (top row in Fig. 4). Particularly interesting are the results obtained for the case with SL angular speed as input. Slopes at low frequencies are +20 dB/decade for the sprung mass acceleration and dynamic tire deflection outputs (pure differentiator), and −20 dB/decade for the dynamic suspension deflection (pure integrator). This confirms the intuition that the SAVGS will be able to provide chassis height and attitude control at frequencies at and below the sprung mass resonance ($f \leq 2$ Hz). At high frequencies, magnitudes drop at a rate of −40 dB/decade for the dynamic suspension and tire deflections, but remain constant for the sprung mass acceleration. This implies that at high frequencies, although the SAVGS will not be able to enhance road holding, it could potentially improve comfort without excessive working space requirements (if the actuator was responsive enough).

2.2.3. Effect of the nominal SL angle

The effect of the nominal SL angle, $\theta_{SL}^{(ne)}$, on the attitude control capabilities of the SAVGS for steady-state conditions was analyzed in Arana et al. (2016). The results shown confirmed the intuitive idea that a nominal angle close to $\theta_{SL}^{(ne)} \approx \theta_{SL}^{(min)} + \Delta\theta_{SL}^{(ne)}$, with $\Delta\theta_{SL}^{(ne)} = 90$ deg, provides the best attitude control performance ($\theta_{SL}^{(min)}$ represents the passive equilibrium configuration, as shown in Fig. 1-a, and $\theta_{SL}^{(min)} + 90$ deg a situation in which the SL is almost perpendicular to the SD). In order to describe the influence of the nominal SL angle on the dynamic response of the SAVGS, the system gains from SL speed to sprung mass acceleration, dynamic suspension and tire deflections are shown in Fig. 5 as a function of $\Delta\theta_{SL}^{(ne)}$. As in the attitude control case, a nominal angle offset, $\Delta\theta_{SL}^{(ne)}$, close to 90 deg leads to the maximum gain. The shape of the Bode plot remains largely unchanged by $\Delta\theta_{SL}^{(ne)}$ but the gain of the system is very sensitive to it, except in the region around $\Delta\theta_{SL}^{(ne)} = 90$ deg. In practice, the SAVGS becomes ineffective at nominal angle offsets close to 0 and 180 deg.

Limitations of active suspensions. Irrespective of the actuator bandwidth, the SAVGS will not be able to provide much comfort improvement at frequencies close to 10 Hz (the wheel hop frequency) due to a zero in the transfer function from $\dot{\theta}_{SL}$ to vertical acceleration of the sprung mass, $\ddot{z}_s$, at that frequency. Similarly, the SAVGS will not be able to reduce suspension deflections at the rattle-space frequency (∼3.5 Hz) due to a zero in the transfer function from $\dot{\theta}_{SL}$ to dynamic suspension deflection, Δl_s, at that frequency. The aforementioned zeros in the transfer functions are compatible with analyses reported in the literature (e.g. (Hedrick & Butsuen, 1990; Smith & Walker, 2000; Smith, 1995; Yue, Butsuen, & Hedrick, 1988)) that deal with performance limits of active suspensions. Active suspensions are subject to some fundamental limitations due to the fact that their action can only be introduced between the chassis and the wheel. In linear system terms, the limitations are seen in a lack of adjustability of terms in the numerators of various transfer functions (Karnopp, 1986). The interested reader is referred to Gillespie (1992), Savaresi, Poussot-Vassal, Spelta, Sename, and Dugard (2010) for an in-depth treatment of the topic.

2.2.4. Suitability of the conventionally linearized model for control synthesis

The conventionally linearized model can be a good representation of the system as long as a sensible damping coefficient is used and external disturbances are not excessively large. The question arises whether this model is valid for a wide enough range of SL positions and whether it is the best choice for control synthesis (the rear suspension of the GT is considered in the following analysis).

According to Section 2.2.2, the nominal SL angle offset has a remarkable effect upon the ability of the SAVGS to affect the dynamic response of the vehicle. With this in mind, it is important to establish whether the multi-body model linearized at the nominal configuration is a good representation of the system when the SL is rotated far from its default position, and therefore whether a control system synthesized for it will be effective for a wide enough range of SL positions.

To answer this question, the first step is to linearize the quarter-car model for a trim state corresponding to the nominal configuration (straight line driving at 100 km/h, nominal payload, nominal single-link angle $\Delta\theta_{SL}^{(ne)} = 90$ deg, nominal suspension position). This model will be referred to from now on as nominal linearized model. Considering no external loads, new equilibria have also been found for SL rotations with respect to the nominal configuration, $\theta_{SL} = \theta_{SL}^{(ne)} + \Delta\theta_{SL}$, and the multi-body model has been linearized for the new trim states. In these new equilibria, suspension deflections and chassis heights differ from those of the nominal configuration. These models will be referred to from now on as updated linearized models. Bode magnitude plots (for various input-output transmission paths) for the new equilibria conditions have been computed with both the nominal and updated models.

Fig. 6 shows the absolute value of the magnitude difference between the transfer functions obtained with the nominal and updated linearized models, divided by the magnitude of the transfer functions calculated with the updated linearized models (expressed as a percentage). From this figure, it is clear that the gains from road velocity and external load to all outputs are quite insensitive to SL angle: with short SLs the changes in installation ratio, and therefore in effective spring rate and damping coefficient, are small and can be safely neglected when synthesizing a controller. On the other hand, the nominal linear model fails to accurately estimate gains from SL speed to all outputs, for SL rotations with respect to the nominal configuration larger than ± 30 deg. Although different controllers could be synthesized for different ranges of operating conditions (gain scheduling), this is not ideal and therefore the following section derives a model that is more robust to SL position changes.

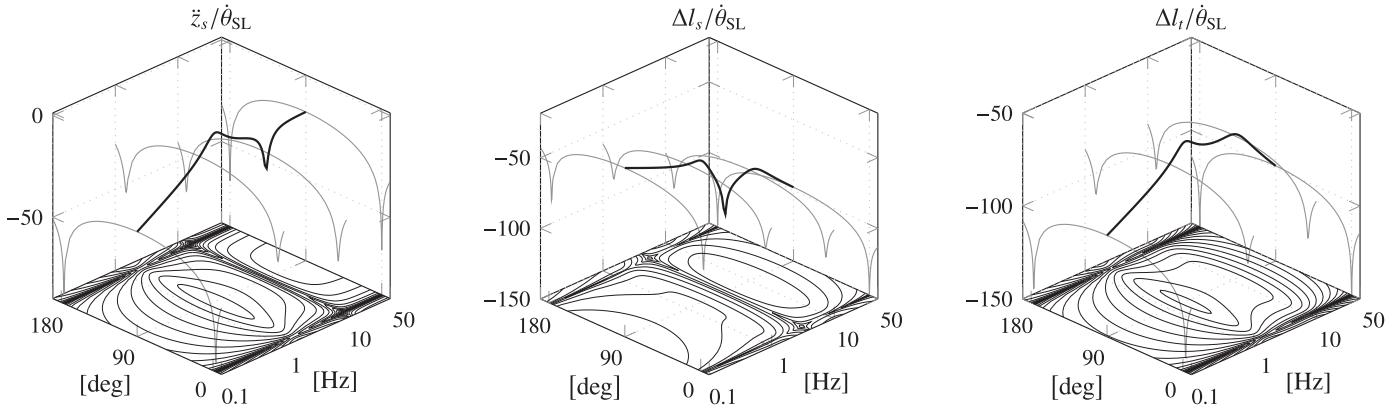

Fig. 5. Magnitude Bode plots for one rear corner of the GT, in dB, from SL speed to sprung mass acceleration (left), dynamic suspension deflection (center) and dynamic tire deflection (right) as a function of frequency and nominal SL angle offset, $\Delta\theta_{SL}^{(ne)}$. Thick black lines correspond to the $\Delta\theta_{SL}^{(ne)} = 90$ deg case. Slices at $f = 0.1$, 1, 10, 50 Hz as well as magnitude contours are also shown in the 3D figures.

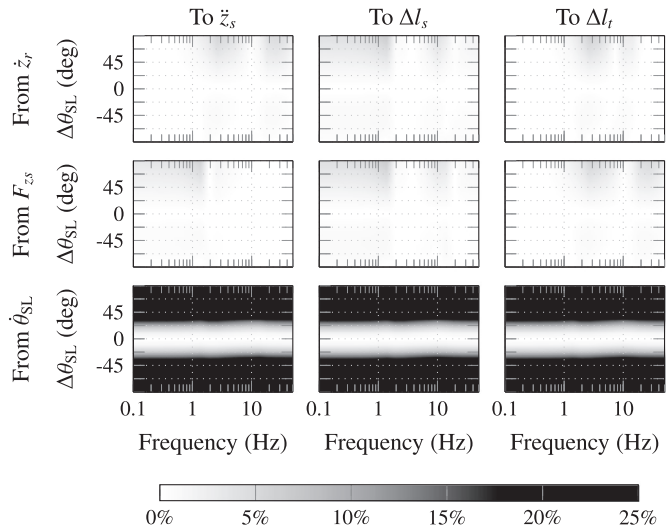

Fig. 6. Relative error (in absolute value) between the gains obtained with the model linearized at the trim state corresponding to $\theta_{SL} = \theta_{SL}^{(ne)}$, and the model linearized at trim states corresponding to $\theta_{SL} = \theta_{SL}^{(ne)} + \Delta\theta_{SL}$. In all cases $\theta_{SL}^{(ne)} = \theta_{SL}^{(min)} + 90$ deg.

2.3. Energy-based linearization of the multi-body model

This section derives a model that removes the main geometric nonlinearity associated with the SL rotation. The concept, depicted in Fig. 7, implies the augmentation of the quarter-car model with a block α^{-1}, in which the effect of the geometric nonlinearity is lumped. As a result, the gains from the control action, u, to the system outputs, $\boldsymbol{o}$, can be made largely independent of the actual SL angle. The path from the external disturbances, $\boldsymbol{w}$, to the measured outputs does not need to be modified as it is already independent of the SL position (as discussed in Section 2.2.4).

The proposed model, shown in Fig. 8, has been derived based on energy considerations and it is an extension of the conventional linear

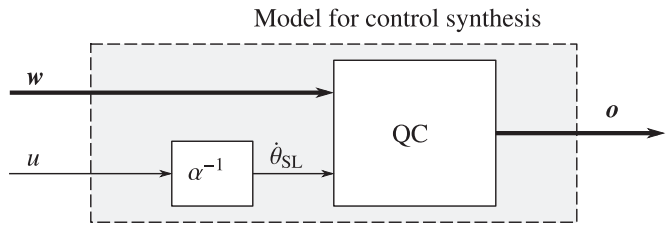

Fig. 7. A model without a strong dependency on SL angle will enable the synthesis of controllers suitable for a wide range of SL angles.

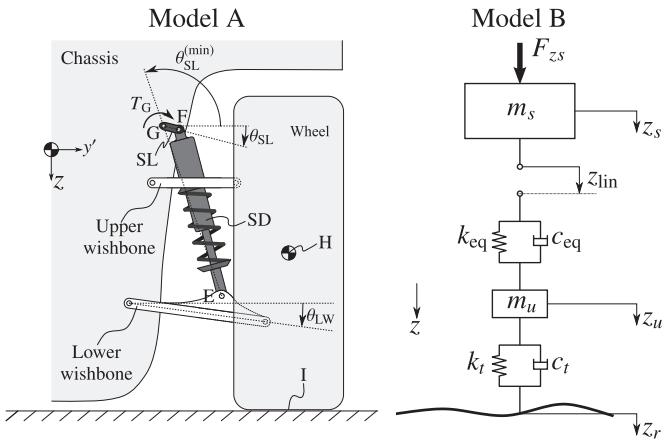

Fig. 8. SAVGS-retrofitted double-wishbone suspension (model A) and representation of the equivalent hand-derived model (model B).

quarter-car model. The vertical displacements of the sprung and unsprung masses in model B, z_s and z_u, are equal to the vertical displacements of the chassis and wheel in model A. As the SL appears in series with the passive SD, its influence on the system dynamics is better incorporated through a displacement input rather than as a force/torque input. Thus, the suspension deflection (i.e. the distance between the sprung and unsprung masses) is now split into two terms: the deflection of the equivalent SD, and the displacement of an equivalent linear actuator, z_{lin}, that accounts for the contribution of the SL.

The power provided by the SAVGS to the rest of the system through the SL (model A) must be matched by the power provided by the equivalent linear actuator to the rest of the simplified quarter-car model (model B). This power balance implies that:

$$T_G\dot{\theta}_{SL} = F_{SD}^{*}\dot{z}_{lin}, \tag{1}$$

where T_G is the torque applied to the SL (model A), $\dot{\theta}_{SL}$ is the angular speed of the SL (model A), F_{SD}^{*} is the SD force (model B), and $\dot{z}_{lin}$ is the speed of the equivalent linear actuator (model B). The SAVGS torque can be obtained by applying the principle of virtual power to the single-link in model A:

$$T_G = -F_{SD}\frac{\partial l_{SD}}{\partial \theta_{SL}}, \tag{2}$$

with F_{SD} and l_{SD} the SD force and length in model A.

Defining R_{SD} as the installation ratio of the SD in model A:

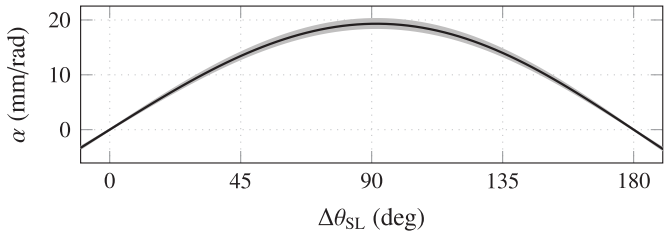

Fig. 9. Evolution of α as a function of SL angle, $\Delta\theta_{SL} = \theta_{SL} - \theta_{SL}^{(min)}$ for the rear suspension of the GT. The gray band indicates the variations of α with suspension travel for maximum wheel displacements of ±50 mm with respect to the nominal equilibrium position.

$$R_{SD} = \frac{\partial l_{SD}}{\partial z_H} = \frac{\partial l_{SD}}{\partial \theta_{LW}} \frac{\partial \theta_{LW}}{\partial z_H}, \tag{3}$$

the relationship between the forces produced by the real and equivalent SD for any trim state is given by:

$$F_{SD}^{*} = R_{SD}\, F_{SD}. \tag{4}$$

Substituting (2) and (4) into (1), the parameter α, that accounts for the geometric nonlinearity of the SL and which is a function of wheel travel and SL angle, can be computed through:

$$\dot{z}_{lin} = -\frac{1}{R_{SD}} \frac{\partial l_{SD}}{\partial \theta_{SL}} \dot{\theta}_{SL} \Rightarrow \alpha = -\frac{1}{R_{SD}} \frac{\partial l_{SD}}{\partial \theta_{SL}}. \tag{5}$$

Terms $\frac{\partial l_{SD}}{\partial \theta_{LW}}$ and $\frac{\partial l_{SD}}{\partial \theta_{SL}}$ can be computed from (14) and (17) in Arana et al. (2016), and $\frac{\partial \theta_{LW}}{\partial z_H}$ depends solely on the passive suspension geometry and can be obtained from a kinematic analysis of the passive suspension.

Fig. 9 shows the evolution of α with SL rotation, $\Delta\theta_{SL} = \theta_{SL} - \theta_{SL}^{(min)}$, for the rear suspension of the GT. The curve is shaped as a negative parabola that crosses zero at $\Delta\theta_{SL} = 0$ deg and $\Delta\theta_{SL} = 180$ deg, when the SL is aligned with the SD, and that reaches ~19 mm/rad at or close to $\Delta\theta_{SL} = 90$ deg. Furthermore, the influence of suspension travel, Δz_H, on α is shown for $\Delta z_H \in [-50, 50]$ mm through gray bands around the nominal case. This effect is reasonably small, with a band half-width of ~4% with respect to the nominal equilibrium case in which $\Delta z_H = 0$.

With the following state variables and system inputs/outputs:

$$\begin{aligned} \boldsymbol{x}^T &= [\dot{z}_s,\ \dot{z}_u,\ \Delta l_s,\ \Delta l_t,\ z_{lin}], \\ \boldsymbol{v}^T &= [\boldsymbol{w}^T,\ u] = [\dot{z}_r,\ F_{zs},\ \dot{z}_{lin}], \\ \boldsymbol{o}^T &= [\ddot{z}_s,\ \Delta l_s,\ \Delta l_t], \end{aligned} \tag{6}$$

the state-space representation for the new model is:

$$\begin{aligned} \dot{\boldsymbol{x}} &= A\,\boldsymbol{x} + B\,\boldsymbol{v}, \\ \boldsymbol{o} &= C\,\boldsymbol{x} + D\,\boldsymbol{v}, \end{aligned} \tag{7}$$

with

$$\begin{bmatrix} A & B \\ C & D \end{bmatrix} = \begin{bmatrix} -\frac{c_{eq}}{m_s} & \frac{c_{eq}}{m_s} & \frac{k_{eq}}{m_s} & 0 & -\frac{k_{eq}}{m_s} & 0 & \frac{1}{m_s} & -\frac{c_{eq}}{m_s} \\ \frac{c_{eq}}{m_u} & -\frac{c_{eq}+c_t}{m_u} & -\frac{k_{eq}}{m_u} & \frac{k_t}{m_u} & \frac{k_{eq}}{m_u} & \frac{c_t}{m_u} & 0 & \frac{c_{eq}}{m_u} \\ -1 & 1 & 0 & 0 & 0 & 0 & 0 & 0 \\ 0 & -1 & 0 & 0 & 0 & 1 & 0 & 0 \\ 0 & 0 & 0 & 0 & 0 & 0 & 0 & 1 \\ -\frac{c_{eq}}{m_s} & \frac{c_{eq}}{m_s} & \frac{k_{eq}}{m_s} & 0 & -\frac{k_{eq}}{m_s} & 0 & \frac{1}{m_s} & -\frac{c_{eq}}{m_s} \\ 0 & 0 & 1 & 0 & 0 & 0 & 0 & 0 \\ 0 & 0 & 0 & 1 & 0 & 0 & 0 & 0 \end{bmatrix}. \tag{8}$$

The equivalent properties of the SD, k_{eq} and c_{eq}, may be computed (for the trim state of interest) from the component properties k and c through similar energy considerations. Imposing that the rate of change of energy stored in the real and equivalent springs must be the same, and that the rate of energy dissipation in the real and equivalent dampers must be equal, the equivalent spring-damper properties can be found through:

$$k_{eq} = k\, R_{SD}^2 - F_{SD} \frac{\partial R_{SD}}{\partial z_H}, \quad c_{eq} = c\, R_{SD}^2, \tag{8}$$

where R_{SD}, F_{SD} and $\frac{\partial R_{SD}}{\partial z_H}$ are computed for the trim state of interest. The partial derivative of the installation ratio with respect to wheel motion is found by differentiating (3). For this, (11) in Arana et al. (2016) is required to obtain $\frac{\partial}{\partial z_H}\left(\frac{\partial l_{SD}}{\partial \theta_{LW}}\right)$.

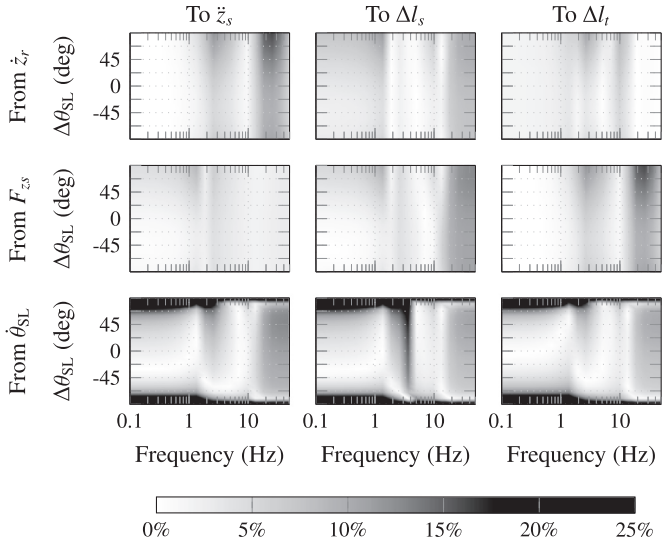

Fig. 10. Relative error (in absolute value) between the gains obtained with the hand-derived model linearized at the trim state corresponding to $\theta_{SL} = \theta_{SL}^{(ne)}$, and the conventionally linearized model linearized at the trim state corresponding to $\theta_{SL} = \theta_{SL}^{(ne)} + \Delta\theta_{SL}$. In both cases $\theta_{SL}^{(ne)} = \theta_{SL}^{(min)} + 90$ deg.

The accuracy of the predictions obtained with this simple model are compared in Fig. 10 with those provided by the updated conventionally linearized models. The only difference between Figs. 10 and 6 is that the model tested is the simple hand-derived linear model with parameters corresponding to $\Delta\theta_{SL}^{(ne)} = 90$ deg instead of the nominal linearized model. For easier comparison with Fig. 6, the same color scale and axes have been used. The differences with respect to the nominal conventionally linearized model are evident. On the one hand, the quality of the approximation suffers slightly for inputs $\dot{z}_r$ and F_{zs}, as well as for input $\dot{\theta}_{SL}$ and small SL rotations. These errors, however, are considered to be acceptable as they remain below 10% in most areas. On the other hand, the range of SL positions for which an acceptable match is achieved is greatly increased from approximately ±30 deg to ±70 deg. This means that the hand-derived linear model represents the system with sufficient accuracy for the whole range of desirable SL rotations, which in general are not limited to $[\theta_{SL}^{(min)}, \theta_{SL}^{(max)}]$ but to $[\theta_{SL}^{(min)} + \Delta\theta_{SL}^{(min)}, \theta_{SL}^{(max)} - \Delta\theta_{SL}^{(max)}]$, with $\Delta\theta_{SL}^{(min)}$ and $\Delta\theta_{SL}^{(max)}$ typically in the 0–30 deg range (Arana et al., 2016) because the effect of the SAVGS on the suspension forces is negligible when the SL is almost parallel to the SD.

In short, the proposed model: 1) is of smaller size than the conventionally linearized model: $A \in \mathbb{R}^{5\times5}$ instead of $A \in \mathbb{R}^{8\times8}$; 2) it approximates the system dynamics reasonably well for the whole range of SL rotations; and 3) it can be easily extended to represent a linear full-vehicle model equipped with the SAVGS. For these reasons, the simpler hand-derived linear model has been preferred over the conventionally linearized model for the synthesis of control algorithms.

3. $\mathcal{H}_\infty$ control synthesis framework

The generalized regulator considered for $\mathcal{H}_\infty$ control synthesis is shown in Fig. 11, where: w represents the exogenous disturbances

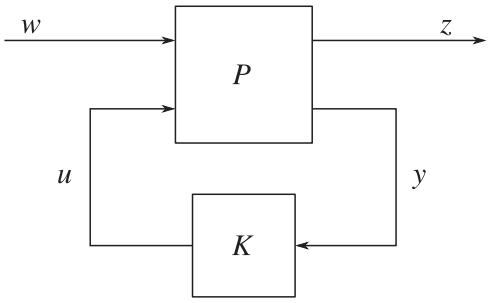

Fig. 11. Schematic of the generalized regulator.

acting on the system, z represents the variables that are to be controlled, y are the measurement signals made available to the controller, and u are the control actions.

The overall transfer function from w to z for the interconnection shown in Fig. 11 corresponds to a lower Linear Fractional Transformation (LFT) (Doyle, Packard, & Zhou, 1991):

$$R_{zw} = \mathcal{F}_l(P, K) = P_{11} + P_{12}K(I - P_{22}K)^{-1}P_{21} \tag{9}$$

The aim of the controller K designed with $\mathcal{H}_\infty$ techniques is to find an admissible controller (i.e. causal, linear, time-invariant, finite-dimensional and that will internally stabilize P) that satisfies the infinity norm objective (Green & Limebeer, 1995):

$$\|R_{zw}\|_\infty < \gamma. \tag{10}$$

That is, the maximum gain from w to z in the whole frequency range, which is given by:

$$\left\|R_{zw}\right\|_\infty = \sup_\omega \bar{\sigma}(R_{zw}(j\omega)), \tag{11}$$

with $\bar{\sigma}(R_{zw}(j\omega))$ representing the maximum singular value of R_{zw} at any given frequency ω, needs to be bounded by a suitably small real number γ.

The $\mathcal{H}_\infty$ controller, K, is synthesized according to standard methods (see for example (Green & Limebeer, 1995; Zhou & Doyle, 1998)).

For our purposes it can be obtained using MATLAB's `hinfsyn` (the Riccati option works best in this case), which calculates the $\mathcal{H}_\infty$ controller solving two Riccati formulae described in Glover and Doyle (1988), Doyle, Glover, Khargonekar, and Francis (1989). In their derivation, it is assumed that the plant has been simplified through loop-shifting, and the resulting controller $\widetilde{K}$ can be reverse-transformed to obtain the controller for the original problem (Safonov, Limebeer, & Chiang, 1989). All these transformations are performed automatically by MATLAB.

The exogenous disturbances, control objectives, measurements and control actions considered for the control synthesis are covered in Sections 3.1–3.4.

3.1. Exogenous disturbances, w

Three external inputs have been considered for the control synthesis: rate of change of road height, vertical load transfer and exogenous position command for the SL. Initially, measurement errors were also included as external disturbances in the synthesis phase. However, sufficient robustness against measurement noise was achieved even when not including these signals when synthesizing the control and therefore they were finally dropped from the design scheme.

The rate of change of road height, $\dot{z}_r$, represents the main exogenous disturbance acting on the suspension system. Individual road bumps, potholes and general road unevenness can introduce large amounts of energy in a wide range of frequencies (according to (ISO, 1995), spatial frequencies in the 0.01–10 cycles/m range should be considered). Significant changes in vertical tire force as well as suspension deflection and sprung mass acceleration arise as this energy is transmitted from the wheel to the chassis.

Load transfers arising from longitudinal and/or lateral vehicle accelerations are captured in the model by an external vertical force, F_{zs}, acting on the sprung mass. This force causes vertical motions of the sprung mass, which in turn result in suspension deflections and changes in vertical tire forces. Typically, pitch and roll natural frequencies are in the 1–3 Hz range, and therefore it is expected that most input energy will be concentrated in this frequency band.

Finally, the SL position command provided by higher level controllers has also been considered as an exogenous input. This is the angle from which the SAVGS is asked to operate and is referred to as $\theta_{\mathrm{SL}}^{(\mathrm{e})}$ or $z_{\mathrm{lin}}^{(\mathrm{e})}$ when dealing with SL rotations and equivalent linear displacements, respectively.

Thus, the exogenous disturbances are weighted versions of the physical (denoted by tilde) signals:

$$\widetilde{\boldsymbol{w}}^T = [z_{\mathrm{lin}}^{(\mathrm{e})}, \dot{z}_r, F_{zs}]. \tag{12}$$

3.2. Control objectives and constraints, z

In this paper, the two main control objectives considered are 1) to improve ride comfort and 2) to increase tire grip. These two aspects of suspension performance are commonly quantified in the quarter-car context through the vertical acceleration of the sprung mass (comfort), and vertical tire force variations or dynamic tire deflections (grip). As already discussed in Section 2.2.2, these objectives are not independent. There are invariant points and slope constraints (interpolation conditions (Türkay & Akçay, 2008)) in the transfer functions of interest, as well as performance trade-offs because once one of the transfer functions from road velocity to either sprung mass acceleration or tire deflection is determined, the other one is automatically fixed. Here, both objectives have been maintained in the synthesis phase to facilitate shaping their relative importance in different frequency regions through the application of individual frequency weights. A third control objective included in the synthesis scheme is the tracking of exogenous SL position commands.

The performance of the suspension system deteriorates if the bump stops are hit and therefore it is important to ensure that maximum suspension travel is maintained within allowable limits. As opposed to most active suspensions, in which actuators with large strokes act in parallel with the SD, the short SL of the SAVGS acts in series with the SD and has a limited capacity to increase suspension travel beyond allowable bounds. As a consequence, this control objective has been dropped from the synthesis stage (this will be validated by simulation results presented in Section 4).

Finally, the aforementioned objectives need to be achieved with sensible levels of actuation effort. Actuation torque and power cannot be penalized in this linear framework, but rotation and angular speed of the SL can and have been penalized through z_{lin} and $\dot{z}_{\mathrm{lin}}$, respectively.

Thus, the controlled variables are weighted versions of the physical signals:

$$\widetilde{\boldsymbol{z}}^T = [z_{\mathrm{lin}}^{(\mathrm{e})} - z_{\mathrm{lin}}, \ddot{z}_s, \Delta l_t, z_{\mathrm{lin}}, \dot{z}_{\mathrm{lin}}]. \tag{13}$$

3.3. Measurements, y

There is a large number of possible combinations of measurement signals (Van De Wal, Philips, & De Jager, 1998) and the actual selection may limit the theoretical performance of the active suspension (Smith, 1995). Here, signals made available to the controller have been chosen based on the expected availability of sensors. In particular, two uniaxial accelerometers (one for the vertical acceleration of the

sprung mass and one for the vertical acceleration of the wheel center), one LVDT linear position sensor or potentiometer (to measure suspension deflection) and one encoder (to measure angular position of the SL) have been considered. The signals fed to the controller in the synthesis stage are:

$$\boldsymbol{y}^T = [\dot{\Delta l}_s,\ \ddot{z}_u,\ \ddot{z}_s,\ z_{\text{lin}}^{(e)} - z_{\text{lin}}], \tag{14}$$

where $\dot{\Delta l}_s$ can be obtained by differentiating the reading provided by the LVDT.

3.4. Control action, u

The equivalent SL speed has been preferred as control output over the equivalent displacement because (1) the linear model requires actuation speed to compute damper forces, and (2) this simplifies the application of the control to configurations in which the SL angle differs from that of the trim state. As the control command,

$$u = \dot{z}_{\text{lin}}^*, \tag{15}$$

cannot be perfectly tracked by the actuators in each corner of the vehicle, a transfer function that represents the dynamics of the actuator and its already described (Arana et al., 2015) inner control loops (IL) has been introduced in the synthesis framework:

$$\dot{z}_{\text{lin}} = P_{\text{IL}}\ \dot{z}_{\text{lin}}^*. \tag{16}$$

However, the system response is very nonlinear and therefore a single linear transfer function cannot capture the real system dynamics. The tracking problem can be particularly acute for rapidly changing speed commands, for large SL rotations and for cases in which the actuator is limited by low torque and current constraints. Fig. 12 highlights these facts and shows the relationship, in the frequency domain, between $\dot{z}_{\text{lin}}^*$ and $\dot{z}_{\text{lin}}$ for the undisturbed quarter-car model and various operating conditions. Results presented in Fig. 12 were obtained with model A for a rear suspension of the GT with $\theta_{\text{SL}}^{(\text{ne})} = \theta_{\text{SL}}^{(\text{min})} + 90$ deg. Without any other external disturbances, the reference speed for the SL, $\dot{z}_{\text{lin}}^*$, was changed sinusoidally and frequencies were swept from 0.1 Hz to 50 Hz. Three amplitudes for the equivalent linear displacement reference, z_{lin}^*, were considered. These amplitudes, in terms of peak-to-peak SL rotation, correspond approximately to 1, 7 and 22.5 deg and were the same for all frequencies considered.

For small z_{lin} amplitudes and peak actuator limits, the actuator and its control loops can be accurately represented by the first order low-pass filter

$$P_{\text{IL}} = \frac{1}{s/(2\pi\ 17.8) + 1}. \tag{17}$$

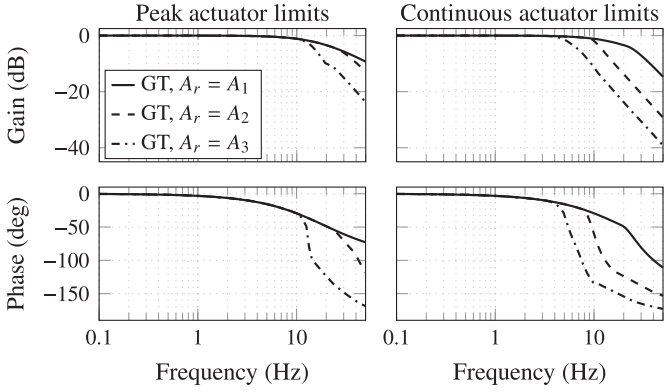

Fig. 12. Gain and phase delay from $\dot{z}_{\text{lin}}^*$ to $\dot{z}_{\text{lin}}$. Results are shown for three levels of relative displacement amplitude $A_r = |z_{\text{lin}}^*|/z_{\text{lin}}^{(\text{max})}$: A_1=0.01, A_2=0.06 and A_3=0.2 which correspond to SL peak-to-peak reference angular motions of 1, 7 and 22.5 deg. These values refer to the reference angular motions. The actual angular amplitudes achieved by the actuator greatly depend on the frequency and torque limits considered.

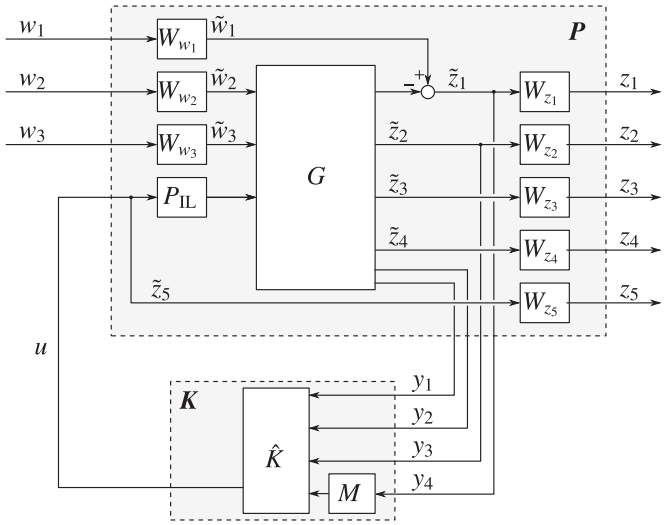

Fig. 13. Interconnection for controller synthesis.

This will be the assumption in this paper. However, as z_{lin} amplitudes increase, the corner frequency is reduced, the falling slope of the gain at high frequencies becomes steeper and the response becomes more erratic (particularly with continuous torque and current limits).

3.5. System interconnection

The interconnection considered for control synthesis is shown in Fig. 13, where nomenclature and signal labeling is compatible with what has been described so far. The performance weight W_{z1} cannot include integral action, as this would imply that s=0 would be an uncontrollable pole of the feedback system (Zhou & Doyle, 1998). However, this problem is overcome and integral action can be included in W_{z1} (and therefore zero steady-state error can be achieved) by filtering the measurement of the exogenous command tracking error with a transfer function M that includes a free integrator. Thus, controller $\widehat{K}$ is obtained using `hinfsyn`, and the final controller, K, is computed by incorporating the effect of M as shown in Fig. 13.

Input and output weights, W_w and W_z, are block diagonal matrices with diagonal terms W_{w_1} to W_{w_3} and W_{z_1} to W_{z_5} that are selected to scale physical quantities (denoted by tilde) and to shape the relative importance between signals in different frequency regions:

$$\tilde{\boldsymbol{w}} = W_w\,\boldsymbol{w}, \quad \boldsymbol{z} = W_z\,\tilde{\boldsymbol{z}}. \tag{18}$$

3.6. Selection of frequency weights

Although there are some general guidelines for the selection of weights in the context of $\mathcal{H}_\infty$ control (see for example the attempts in (Lundström, Skogstad, & Wang, 1991) and (Beaven, Wright, & Seaward, 1996)), and even intelligent methodologies have been used to help the engineer in this process (Do, Sename, Dugard, & Soualmi, 2011), it is clear from the numerous publications dealing with active suspension control that there is not an obvious or unique procedure to select them.

3.6.1. Aims

The $\mathcal{H}_\infty$ controller aims to reduce the maximum gain of the closed loop system augmented with the frequency weights, and therefore these weights must be designed so that the relevant input-output paths dominate in the frequency ranges of interest. The control objectives considered in this work can be summarized as follows: (1) the tracking of the exogenous SL position command should be prioritized at low frequencies but should be negligible at high frequencies; (2) the

reduction of sprung mass acceleration should be prioritized in the 1–10 Hz frequency range, where humans are most sensitive to vibrations; (3) the reduction of gains from external vertical force as well as of gains to dynamic tire deflection should be attempted in the 1–5 Hz frequency range; (4) the actuation effort should be concentrated below 10 Hz.

3.6.2. Tuning process

Although the control synthesis stage is inherently iterative and it involves some level of trial and error, the selection of frequency weights should not be performed blindly. Here, the singular value decomposition (SVD) and the Bode plots for the open-loop and closed-loop systems have been effectively used to inform the selection of frequency weights. Given the $m \times p$ transfer matrix for the plant, R_{zw}, with m=5 the number of controlled outputs and p=3 the number of exogenous disturbances, the SVD of R_{zw} at any given frequency ω is given by:

$$R_{zw}(j\omega) = U(j\omega)\Sigma(j\omega)V(j\omega)^H, \tag{19}$$

where U and V are square matrices of size $m \times m$ and $p \times p$ whose columns have unit $\mathcal{L}_2$ norm and are the singular output and input vectors, H denotes the conjugate transpose, and Σ is an $m \times p$ diagonal matrix with $r = \min(m, p)$ nonzero, positive singular values $\sigma_1 \geq \sigma_2 \geq \ldots \sigma_r > 0$ and $\sigma_q = 0 \ \forall\, q > r$. The singular values represent the gains of the system, and the input and output singular vectors are the associated input and output directions. For example, $\sigma_1(j\omega) = \bar{\sigma}(j\omega)$ is the largest gain in the system at the frequency ω, the first column of $V(j\omega)$ is the input direction with the largest amplification at that frequency and the first column of $U(j\omega)$ is the output direction in which the inputs are most effective. By comparing the SVD of the open-loop (with and without augmenting the plant with the frequency weights) and closed-loop systems, the number of iterations required to obtain a controller that effectively tackles the control aims from Section 3.6.1 can be greatly reduced.

Regarding the characteristics of the frequency weights, it is worth noting that although high order weights allow more flexibility in shaping the response of the system, they also lead to higher order controllers (Bibel & Malyevac, 1992) and complicate the tuning process. Here the selection process began considering scalar weights for all signals, and frequency-dependency was added carefully when it made sense from the physical and control design points of view. Eventually, good performance has been obtained with a mix of scalar and first order frequency weights. In particular, the input weights selected for the rear suspension of the GT are given by:

$$W_{w1} = 0.02, \quad W_{w2} = 0.25, \quad W_{w3} = 1000, \tag{20}$$

where the gains are related to the maximum expected input values. The in-loop block M has been selected according to:

$$M = \frac{s/(2\pi\ 1) + 1}{s}, \tag{21}$$

and the output weights are:

$$W_{z1} = \frac{1/0.0035}{s}, \quad W_{z2} = \frac{1/0.9}{s/(2\pi\ 10)+1}, \quad W_{z4} = 1,$$
$$W_{z3} = \frac{1/0.005}{s/(2\pi\ 5)+1}, \quad W_{z5} = \left(\frac{1}{0.1}\right)\frac{s/(2\pi\ 15)+1}{s/(2\pi\ 100)+1}, \tag{22}$$

where the inverse of the DC gains are related to the maximum expected output values. The weight for exogenous SL position command tracking is a pure integrator, for sprung mass acceleration and dynamic tire deflections are first order low-pass filters with cut-off frequencies of 10 Hz and 5 Hz, respectively, and the penalty for the control effort $\dot{z}_{\text{lin}}$ increases from 10 at frequencies below 15 Hz to ~65 at frequencies above 100 Hz. The effect of the penalty for the control effort z_{lin} has been found to be almost negligible in this case, but has been left here for completeness. The resulting controller has 12 states. Its real time implementation (in discrete time) involves inexpensive matrix-vector product operations at every sampling time and it is therefore straightforward.

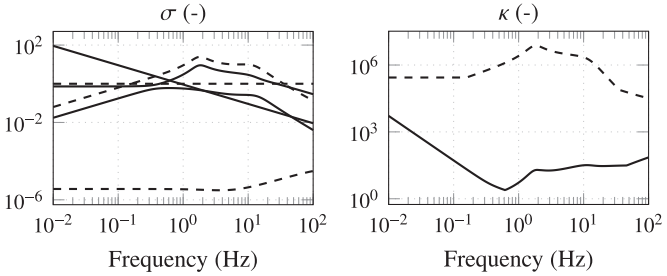

Fig. 14. Singular values and condition number for the open-loop system without (dashed) and with (solid) frequency weights.

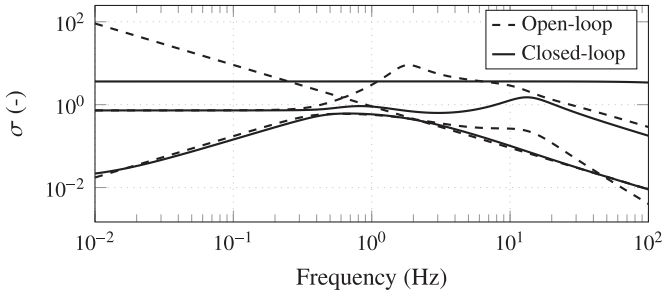

Fig. 15. Singular values for the weighted system.

The singular values and condition number, $\kappa(j\omega) = \bar{\sigma}(j\omega)/\underline{\sigma}(j\omega)$, are shown in Fig. 14 for the open-loop system representing the rear suspension of the GT, with and without the selected frequency weights. The singular values for the weighted open-loop and closed-loop systems are compared in Fig. 15. Finally, the associated input and output directions for the open-loop system with and without weights, and for the closed-loop weighted system are presented in Fig. 16. These are particularly useful during the tuning of the weighting functions: the $\mathcal{H}_\infty$ controller tries to minimize the maximum singular value throughout the frequency range and therefore it is key to identify not only the system gains (singular values) for each frequency but also their associated input-output paths. This information has been used effectively to tune the frequency weights so that the path(s) for which we want to reduce the gain in any given frequency range do actually dominate in that frequency region for the weighted, open-loop system.

In the unscaled open-loop system, the path from exogenous SL position command to tracking error dominates at low and high frequencies, and road velocity to sprung mass acceleration dominates in the mid-frequency range. Gains of the path from the external vertical force to dynamic tire deflection are negligible in comparison throughout the frequency range (dashed line in Fig. 14 in the vicinity of 10^{-6}). Through appropriate selection of the frequency weights, the gains of the systems for different paths and frequency regions can be adjusted so that the control priorities described in Section 3.6.1 are addressed by the synthesized controller. In the weighted open-loop system, exogenous SL position command and tracking error dominate only at frequencies below 0.6 Hz. In the 0.7–30 Hz range, the main input direction transitions from 75% vertical road velocity and 25% external force, to 100% external force, and the main output direction from 75% sprung mass acceleration and 25% tire deflection to 100% sprung mass acceleration (Fig. 16, row 1, columns 3 and 4). The penalty on $\dot{z}_{\text{lin}}$ prevents the SAVGS from doing much above the wheel-hop frequency, and the selected weights reduce the condition number in the 0.1–100 Hz range by 3–5 orders of magnitude (see Fig. 14).

The closed-loop system displays a much more interlinked response than the open-loop system. The maximum singular value remains practically constant in the frequency range of interest, but the input-output path associated with it varies significantly. Generally speaking, sprung mass acceleration, exogenous SL position command tracking error and SL speed are the dominant outputs. Tire deflection also has

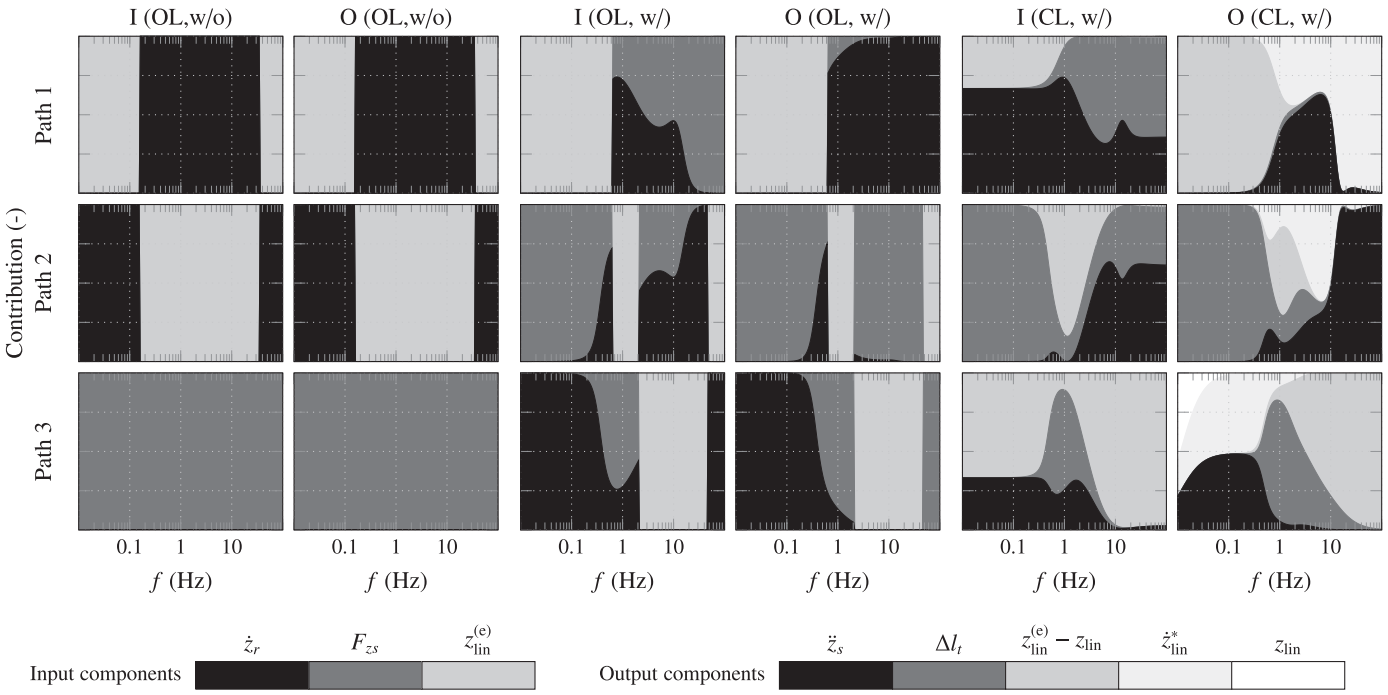

Fig. 16. Singular vector components: contributions to the input (I) and output (O) singular vectors for the open-loop (OL) and closed-loop (CL) systems with (w/) and without (w/o) frequency weights. The vertical distance shown in a particular color at any given frequency represents the proportion of the input (or output) vector length due to a particular input (or output) component. The composition of the input and output singular vectors, together with the magnitude of their associated singular values, has been used to force the $\mathcal{H}_\infty$ controller to focus on reducing the desired input-output gains in various frequency regions. Paths 1–3 are associated with singular values $\sigma_1(j\omega)$ to $\sigma_3(j\omega)$ shown in Figs. 14 and 15. At any given frequency, $\sigma_1(j\omega)$ is the largest singular value and path 1 (top row) the associated input-output path.

some significance, but z_{lin} appears only at low frequencies in the path associated with the minimum singular value (see Fig. 16, columns 5 and 6).

The Bode magnitude plot for the synthesized controller is shown in Fig. 17. As desired, the relative importance of the gain for exogenous SL position tracking error is largest at low frequencies. Control gains, except the one applied to the unsprung mass acceleration, peak around the natural frequency of the sprung mass and roll off at high frequencies.

Finally, the predicted Bode magnitude plots for the open-loop and closed-loop unscaled systems are compared in Fig. 18 and indicate that the control objectives are, at least in the linear world, properly tackled by the synthesized controller. To summarize, the following is achieved: 1) no steady-state error for exogenous SL position tracking; 2) significant reductions in sprung mass acceleration and dynamic tire deflection for road disturbances below the wheel hop frequency (~10 Hz); and 3) significant reductions in sprung mass acceleration and dynamic tire deflection for load transfers below the pitch and roll natural frequencies (~3 Hz). The simulation results obtained with the nonlinear quarter-car and full-car AutoSim models are presented in Section 4 and are used to discuss the suitability of the proposed control.

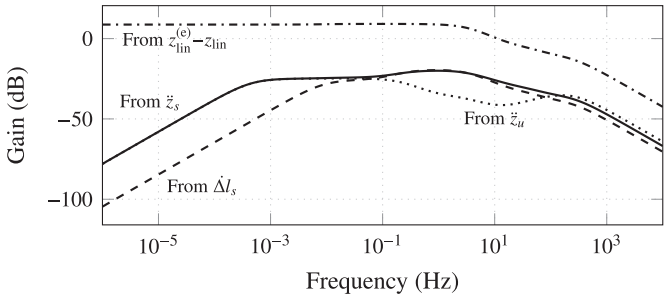

Fig. 17. Bode diagram for controller K for a rear suspension of the GT.

4. Simulation results

Extensive testing has been performed with the nonlinear quarter-car model in order to assess the performance of the SAVGS as well as the quality of the control synthesized in Section 3. Results presented in this section cover three main scenarios: 1) low-speed (20 km/h) driving over a smooth speed bump (sinusoidal profile, 5 cm high and 2 m long); 2) sudden but smooth vertical load transfer (50% of nominal tire load) when driving at 100 km/h; and 3) cruising at 100 km/h for 10 km over three random road profiles representative of very good to poor roads (classes A to C shown in Fig. 3 (ISO, 1995)).

4.1. Control implementation

Results presented have been obtained corrupting all measurements with additive Gaussian white noise and subsequently filtering them with first order low-pass filters with a cut-off frequency of 200 Hz. Noise levels have been estimated based on the official specifications (given as a percentage) of real sensors and it has been assumed that actual noise values are within the official specifications for 99.7% of the time (i.e. that the official specification equals three times the standard deviation of the noise distribution). The standard deviations considered for each measurement signal are: 0.15/3 m/s^2 for $\ddot{z}_s$, 0.30/3 m/s^2 for $\ddot{z}_u$ (larger than for $\ddot{z}_s$ because an accelerometer with a larger full scale range is required), 0.001/3 m for Δl_s, and 0.01/3 rad for $\theta_{\text{SL}}^{(e)} - \theta_{\text{SL}}$. As already mentioned, the performance of the synthesized controller does not deteriorate by any significant amount due to these levels of noise.

Another difference with respect to the interconnection used for control synthesis is that, for convenience, the exogenous position command for the actuator and the tracking error have been computed based on SL angular positions rather than on the equivalent linear displacement. Thus:

$$y_4 = \frac{1}{s/(2\pi\ 200) + 1}\left(\frac{z_{\text{lin}}^{(\max)}}{\pi/2}\right)[\theta_{\text{SL}}^{(e)} - (\theta_{\text{SL}} + N)], \tag{23}$$

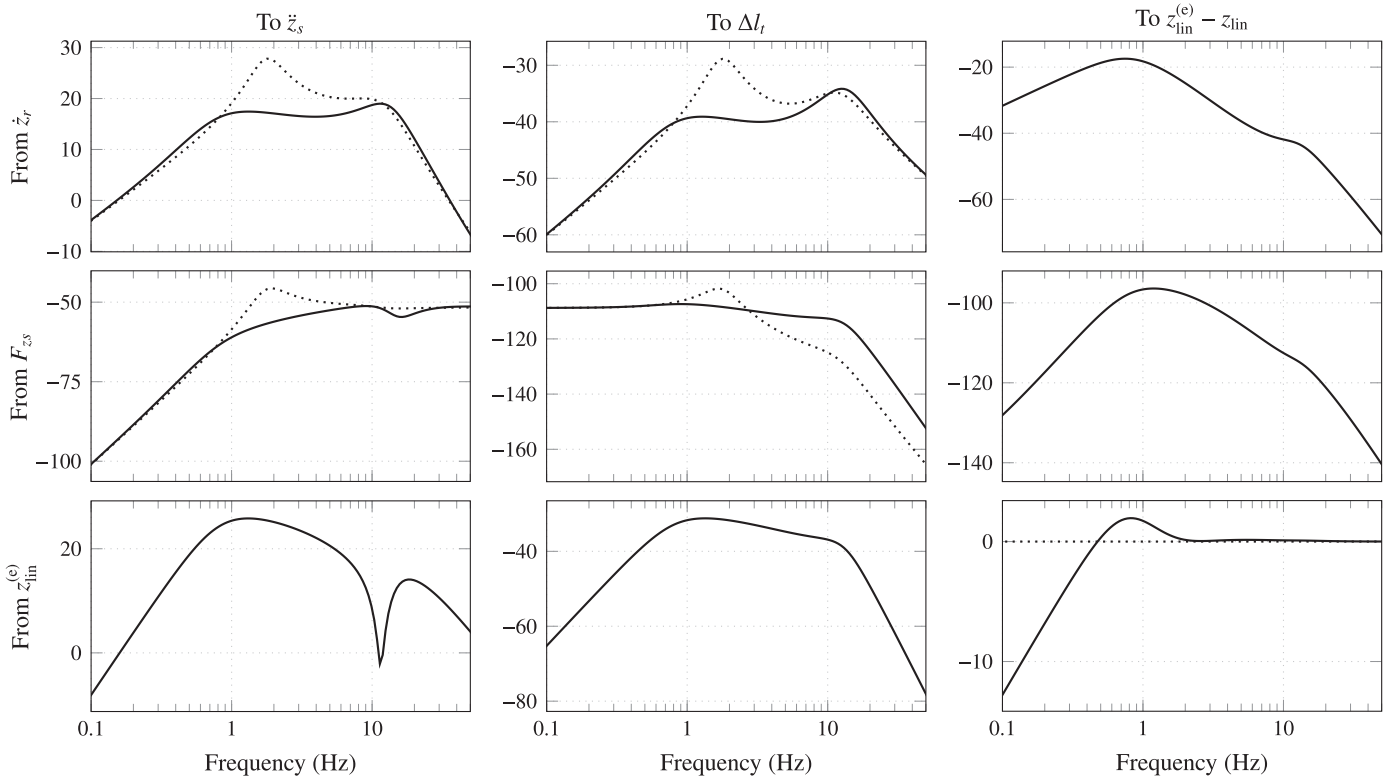

Fig. 18. Comparison of open-loop (dotted) and closed-loop (black) Bode magnitude plots (in dB) for a rear suspension of the GT.

where N represents the Gaussian noise and the factor $\frac{\dot{z}_{\text{lin}}^{(\max)}}{\pi/2}$ scales, approximately, the tracking error from SL angle to equivalent actuator displacement.

Finally, the control input, which represents the reference linear speed for the equivalent linear actuator, $\dot{z}_{\text{lin}}^{*}$, has been converted to reference angular speed for the SL through

$$\dot{\theta}_{\text{SL}}^{*} = \alpha^{-1}\, \dot{z}_{\text{lin}}^{*}, \tag{24}$$

where α is computed on-line through (5) from the (noisy and low-pass filtered) SL position and suspension travel measurements. To avoid excessively large $\dot{\theta}_{\text{SL}}^{*}$ values when the SL is aligned with the SD, α has been constrained to be greater than 0.001 m/rad.

4.2. Quarter-car simulation results

All graphs presented in this section correspond to the rear suspension of the GT.

4.2.1. Individual events—smoothed bump and load transfer

The exogenous position command has been chosen in this case as $\theta_{\text{SL}}^{(e)} = \theta_{\text{SL}}^{(\min)} + 120$ deg in order to illustrate that: 1) for high obstacles, a large exogenous command angle leads to a better usage of the range of SL motions; and that 2) the controller synthesized with the simplified hand-derived model is effective far from the default $\Delta\theta_{\text{SL}} = 90$ deg position.

Fig. 19 shows the time series for the smoothed road bump event. The first three graphs compare the evolution of sprung mass acceleration, vertical tire force and suspension deflection between the benchmark passive suspension and the SAVGS-retrofitted quarter-car. Very significant improvements are achieved simultaneously in all these variables, which is remarkable considering the severity of the bump. To give some context to these results, (van der Sande et al., 2013) reported results for another road bump, only 3 cm high, that led to sprung mass accelerations of the passive vehicle of approximately 2.5 m/s^2 (as opposed to the 7.4 m/s^2 reached in the case considered here). In their case, the active suspension reduced peak sprung mass acceleration by 53%, but suspension deflection and tire force were damaged. In the SAVGS case, improvements in terms of RMS values

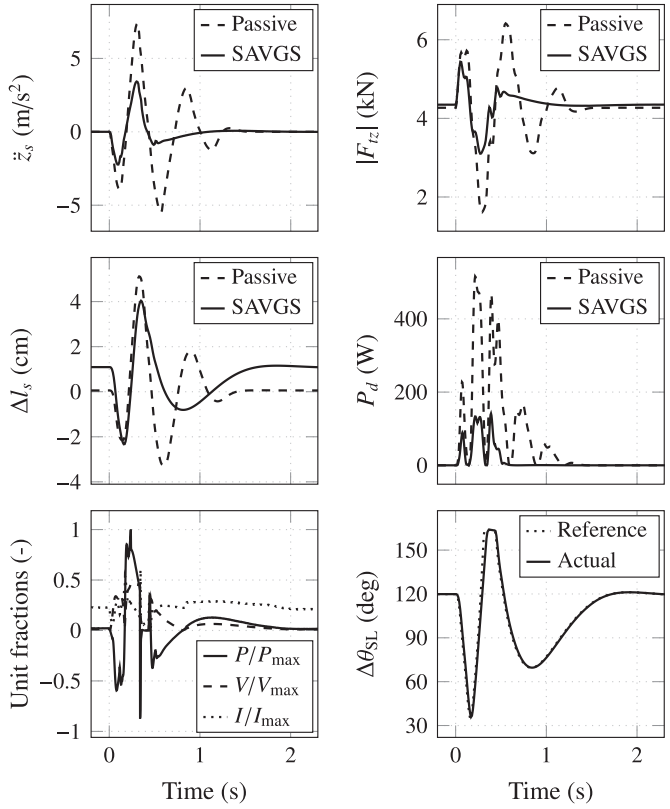

Fig. 19. Simulation results for the rear suspension of the GT with peak actuator limits and $P_{\max} = 1.5$ kW when driving over a 5 cm high and 2 m long speed bump at 20 km/h.

Table 1
Ratio of vertical acceleration, tire force and suspension travel obtained with the SAVGS, over those obtained with the passive suspension during the road bump and load transfer events. Ratios have been computed for root mean square (RMS) and peak values. Ratios corresponding to simulations in which the maximum allowable actuation torques were limited to the peak (ratios shown without brackets) and continuous (ratios shown in brackets) actuator limits are presented.

Parameter	Measure	Road bump	Load transfer
$\ddot{z}_s$	RMS	0.371 (0.546)	0.358 (0.545)
	Peak	0.464 (0.670)	0.380 (0.641)
ΔF_{tz}	RMS	0.391 (0.592)	0.664 (0.762)
	Peak	0.470 (0.736)	0.805 (0.940)
Δl_s	Peak	0.789 (0.612)	0.742 (0.735)

are approximately 63% for sprung mass acceleration and 61% for vertical tire force. Moreover, maximum suspension travel is reduced by 21% with respect to the passive case. A whole summary of RMS and peak ratios with respect to the passive system are provided in Table 1 for peak and continuous actuator limits. The fourth plot in Fig. 19 depicts the power dissipated in the passive damper. In the passive suspension, 500 W are exceeded whereas in the SAVGS case the peak value remains below 150 W. The low levels of power dissipation indicate that there is potential for effective energy regeneration. Moreover, the reduced power dissipation (and therefore heat generation) in the passive dampers may affect the design choices made in their development. The fifth plot shows that power, voltage and current constraints have been respected at all times. Finally, the sixth plot shows the reference and actual SL angular positions. Starting from the constant 120 deg exogenous position command, the motion of the SL is smooth throughout. A minimum angle of approximately 30 deg is reached, close to the point where additional rotations would only have minor effects on the suspension forces, and after the bump absorption the SL angle increases quickly. The allowable range of motion is fully utilized, as demonstrated by the position reference saturation at approximately 160 deg. Once the bump is over, the SL returns to the exogenous position command without activating any undesirable dynamics.

Fig. 20 shows similar time series but for one cycle of a sinusoidal load transfer. The external force peaks at 50% of the nominal vertical tire force and the application period is 0.4 s. That is, $F_{zs} = 2132\sin(2\pi\ 2.5\ t)$ for $t \in [0, 0.4]$. Conservative actuator limits (i.e. continuous actuator limits and a lower power consumption limit of 500 W) have been considered, as load transfer is a common event. Results are as good as for the road bump regarding sprung mass acceleration and slightly worse, but still better than the passive, in terms of vertical tire force variations and suspension travel. The low power and torque limits imposed in this case lead to slower SL motions and more reliance on power dissipation in the passive dampers. RMS and peak ratios with respect to the passive suspension vehicle are summarized in Table 1 for continuous and peak actuator limits.

Finally, the torque applied by the actuator to the SL is shown in Fig. 21 against the SL speed. This confirms that the torque and speed constraints for the actuator are respected.

4.2.2. Random road profiles

Three 10 km long road sections have been generated and used to test the SAVGS in typical uneven road surface conditions corresponding to a good highway, an average quality road and a poor quality road (roads A to C in Fig. 3). All simulations have been performed assuming a constant forward vehicle speed of 100 km/h, a nominal angle offset $\Delta\theta_{SL}^{(ne)} = 90$ deg, continuous actuator limits and a maximum power consumption of 500 W. Fig. 22 shows 5 s long samples of simulation results for roads A and C. The PSDs for sprung mass acceleration and vertical tire force are presented in Fig. 23, and Table 2 summarizes the main results.

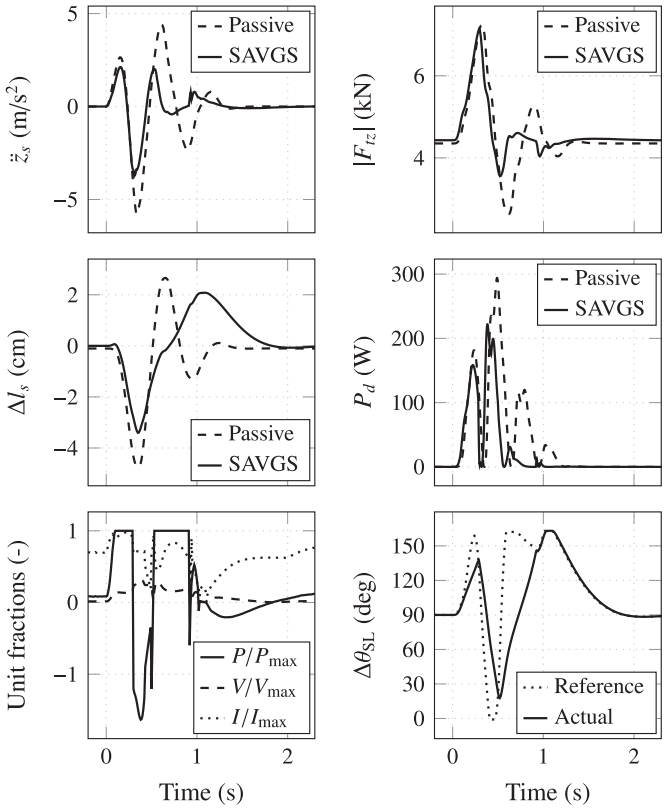

Fig. 20. Simulation results for the the rear suspension of the GT with continuous actuator limits and $P_{max} = 500$ W during a load transfer event when driving at 100 km/h.

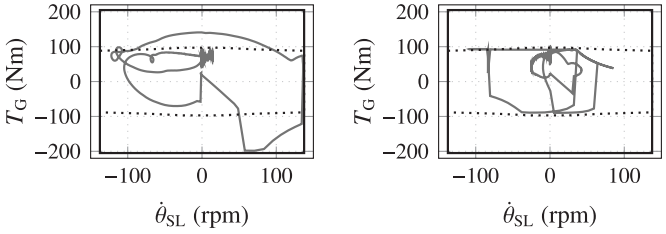

Fig. 21. Output torque-speed operating points for the road bump (left) and load transfer (right) events corresponding to results shown in Figs. 19 and 20, respectively. The peak and continuous actuator limits are shown as solid and dotted black lines, respectively.

The main peak in the PSDs of sprung mass acceleration and vertical tire force, at ~2 Hz, is significantly reduced for the three road classes. The RMS of sprung mass acceleration, which is a good metric for assessing ride comfort, is consistently improved by 15–23%. In the good quality road, vertical tire forces experience a larger amplification at the wheel hop frequency than in the passive system, counterbalancing the improvements achieved at lower frequencies. However, tire force variations are still reasonably small in this case and therefore some degradation is unlikely to be relevant. In the poor quality road the SAVGS significantly reduces the number of events in which the tire leaves the ground. Similarly, peak suspension travel is increased in roads A and B, but this is not relevant as wheel motions are well within limits. In the rougher road (C), the SAVGS reduces peak wheel travel.

In some instances the SL is unable to maintain the required angle with the continuous actuator limits. This is visible in the top row of Fig. 22 at approximately t=1.3 s, when the actuator cannot prevent the SL from being pushed an additional 10 deg towards the passive equilibrium. Also, the controller may be a bit over-aggressive for the continuous actuator limits, as SL position tracking is not as good as in previous cases and the SL reference consistently reaches the maximum and minimum allowable angles in the rough road. Average power

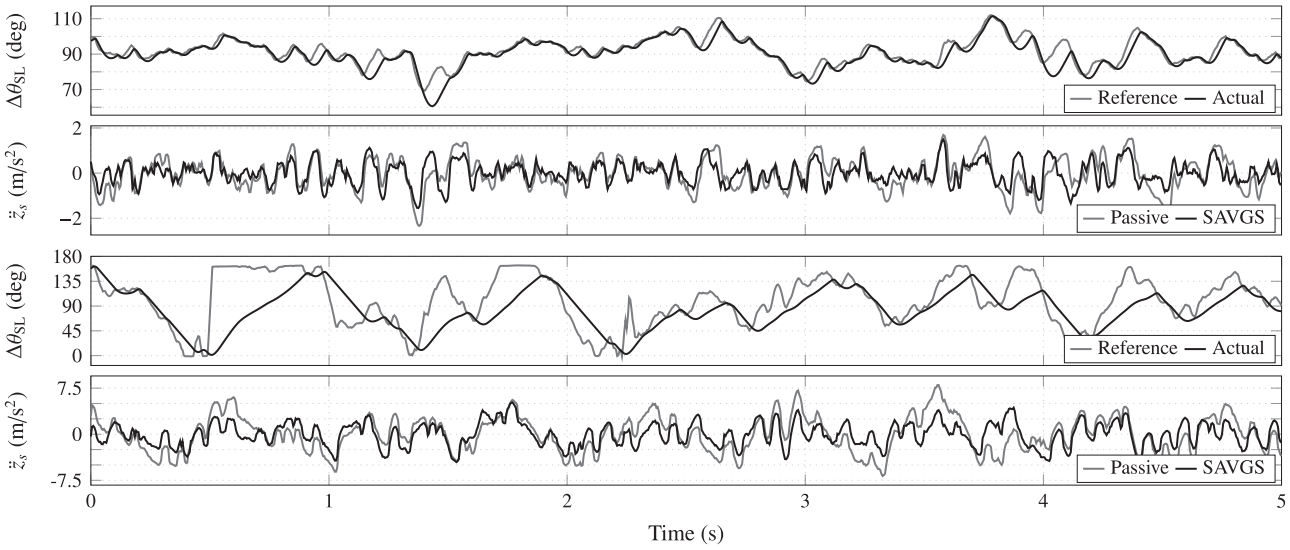

Fig. 22. SL angles and sprung mass acceleration during a 5 s period of road A (top) and road C (bottom) simulations.

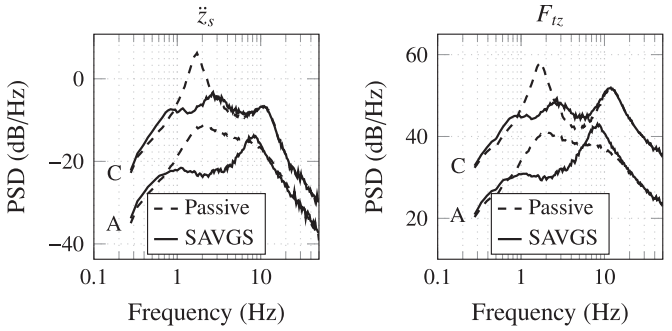

Fig. 23. PSDs of sprung mass acceleration and vertical tire force for the rear suspension of the GT and road classes A and C.

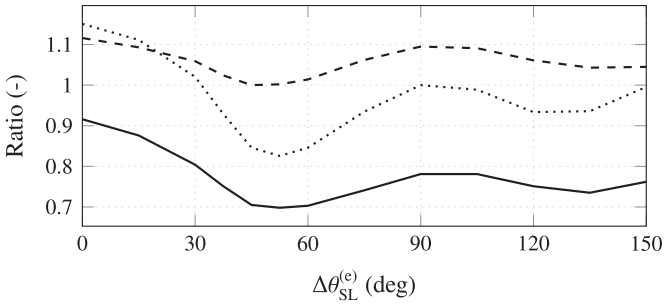

Fig. 24. Influence of constant exogenous position command on SAVGS performance on road A. RMS values for vertical acceleration (solid) and tire forces (dashed) have been normalized with respect to the results obtained with the passive suspension, whereas average power consumption (dotted) has been normalized with respect to the nominal $\Delta\theta_{SL}^{(ne)} = 90$ deg case.

Table 2
Ratio of $\ddot{z}_s$, ΔF_{tz} and Δl_s obtained with the SAVGS, over those obtained with the passive suspension for random roads A to C. Ratios have been computed for RMS and peak values and are shown for continuous actuator limits.

Parameter	Measure	Road A	Road B	Road C
$\ddot{z}_s$	RMS	0.781	0.841	0.768
	Peak	0.838	0.854	0.787
ΔF_{tz}	RMS	1.095	1.049	0.942
	Peak	1.102	1.106	0.784
Δl_s	Peak	1.265	1.120	0.920

consumption is low and increases with road roughness: 89 W, 130 W and 141 W for roads A to C.

These results were obtained considering a constant exogenous position command of $\Delta\theta_{SL} = 90$ deg, position at which the SAVGS has the greatest influence on the suspension response, but also at which actuator demands are greatest. As the continuous torque limits considered are quite stringent, the capability of the actuator to track the position commands provided by the $\mathcal{H}_\infty$ controller suffers. In such conditions, it could be beneficial to operate the SL from a less demanding position. Focusing on the smooth road case (road A), Fig. 24 depicts the influence of the constant exogenous position command on the performance and energy consumption of the SAVGS. The three metrics considered, namely sprung mass acceleration, tire deflection and average power consumption, reach a minimum for $\Delta\theta_{SL} \approx 52.5$ deg. For that case, RMS values of $\ddot{z}_s$ and F_{tz} are 0.698 and 1.002 times those obtained with the passive system (as opposed to 0.781 and 1.095 for the 90 deg case), and the average power consumption is 73 W (as opposed to 89 W for the 90 deg case). The evolution of these metrics with the exogenous position command depends on the level of road disturbances as well as on the capabilities of the actuator. A detailed analysis of this aspect of the SAVGS control is not presented here, but the present discussion suggests that a higher level control could improve the system performance and reduce its power consumption by adjusting the exogenous position command based on the level of road irregularities, forward vehicle speed, actuator constraints, etc.

4.3. Full-car simulation results

Results shown so far indicate that the SAVGS has the potential to significantly improve comfort and road holding, and that a single $\mathcal{H}_\infty$ controller can effectively tackle both objectives when the system is subjected to road bumps, load transfers and irregular roads, irrespective of whether continuous or peak actuator limits are used. In this section, the controllers synthesized for the quarter-car hand-derived model are tested in a full-car nonlinear multi-body model with parameter values representative of a GT as shown in Table A.4 to assess the SAVGS performance under more realistic conditions. The results obtained in this way will serve as basic benchmarks for full-car specific controllers that will be designed in the future.

The vehicle is equipped with front and rear double-wishbone suspensions with linear coil springs, nonlinear damper, massless wishbones and no suspension travel limits, as shown in Fig. 2 and described in Section 2.1. The radial tire forces are obtained assuming

that the tires have a radial spring/damper response with a constant radial stiffness and a constant radial damping coefficient. Lateral and longitudinal tire forces are calculated according to a standard sideslip tire model (Sharp & Bettella, 2003; Sharp, 2004). The model of the rear-wheel-drive vehicle also contains aerodynamic drag and down-forces, powertrain (propeller shaft and rear differential), steering system, and a virtual driver in charge of the longitudinal and lateral motions of the vehicle. More details about this model can be found in Arana et al. (2015).

Results are obtained assuming that the road profiles under the left and right wheels in each axle are the same, and that the rear wheels drive over the same points as the front ones but with some delay determined by the wheelbase. Thus, road irregularities excite the heave and pitch modes of the suspension, but not the roll or warp modes.

Two different controllers are utilized for the SAVGS, one for the rear corners and one for the front corners of the full-car model. Both controllers were synthesized for a quarter-car following the procedure described in Section 3. The controller for the front (rear) corners was tuned for a quarter-car with parameters corresponding to the front (rear) axle of the GT.

Fig. 25 presents relevant time series for the vehicle driving at 20 km/h over the smoothed road bump already described in Section 4.2.1. Negative front-to-rear interactions do not occur in this case and performance improvement is similar to what was achieved with the quarter-car models: 1) Comfort: vertical acceleration of the center of mass of the vehicle (−62.4% in RMS) as well as pitch (θ) acceleration (−58.5% in RMS) are greatly reduced; 2) Road holding: RMS of dynamic vertical tire forces are reduced by 60.7% at the front and by 54.8% at the rear; 3) Ground clearance: improved as the center of mass remains at least 433 mm above the ground and the maximum pitch angle peaks at 1.28 deg (as opposed to 421 mm and 1.54 deg in the passive case); 4) Peak power consumption from the battery does not exceed 4 kW although each of the four actuators is allowed to consume

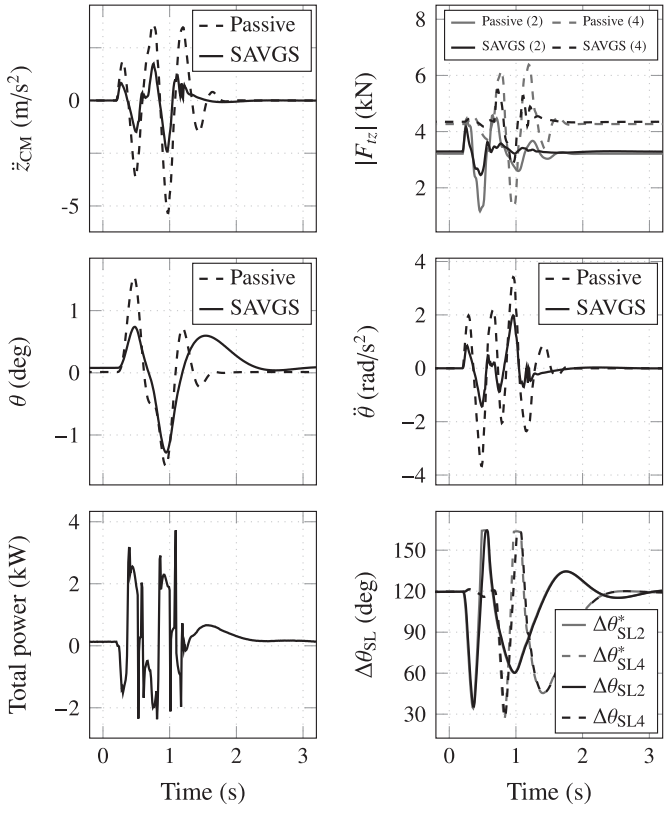

Fig. 25. Full-car GT simulation results for the road bump and peak actuator limits. Numbers 2 and 4 refer to results for the front right and rear right corners, respectively, and * refers to "reference".

Table 3
Results summary for the full-car GT model and random roads A to C. Ratio of vertical acceleration of the center of mass, pitch acceleration, and front and rear tire force variations obtained with the SAVGS, over those obtained with the passive suspension. Ratios have been computed for root mean square (RMS) and peak values and correspond to the continuous actuator limits.

Parameter	Measure	Road A	Road B	Road C
$\ddot{z}_s$	RMS	0.792	0.865	0.786
	Peak	0.916	0.870	0.835
$\ddot{\theta}$	RMS	0.480	0.689	0.921
	Peak	0.698	0.986	0.979
$\Delta F_{tz}^{(\text{front})}$	RMS	1.169	1.250	1.063
	Peak	1.216	1.133	0.929
$\Delta F_{tz}^{(\text{rear})}$	RMS	0.897	0.991	0.957
	Peak	0.919	1.127	0.827

1.5 kW from the high-voltage DC bus.

The full-car has also been tested on the random roads described in the previous section and a summary of the main results is provided in Table 3. The reduction in vertical acceleration of the center of mass of the car is similar to the reduction in sprung mass acceleration in the quarter-car case. Pitch acceleration, $\ddot{\theta}$, is also consistently diminished. Vertical tire forces are improved in the rear axle but this is achieved at the expense of those at the front axle. This highlights that there is scope for control refinement and to find alternative balances between the various control objectives depending on the operating conditions. A slight to moderate increase of tire force variations in exchange for significant comfort enhancement may very well be acceptable when driving in a straight line and at low speeds, but certainly not when driving at high speeds in a winding road.

Finally, the numerical accuracy of the simulations is proved to be satisfactory by computing the power and energy imbalances (as in (Arana et al., 2015)), which are 3–6 orders of magnitude smaller than power and energy flows in the model.

5. Conclusions

This paper has explored the potential of the Series Active Variable Geometry Suspension for comfort and road holding enhancement and has focused on the development of a controller in charge of generating SL position commands for one corner of a GT.

As a first step, a linear hand-derived quarter-car model that includes the SAVGS action through an equivalent linear displacement actuator was presented. Its main advantages over linearized versions of multi-body models are: (1) the extended range of SL angles for which the model is appropriate, (2) its reduced size, and (3) its expandability to the full-car case. Then the $\mathcal{H}_\infty$ framework was applied to synthesize a controller that improves comfort and tire grip. The proposed control is sufficiently robust against measurement noise and leads to simultaneous and significant improvements in comfort and road holding related metrics, as compared to passive suspension, when the GT is subjected to road bumps, load transfers and general road unevenness. The robustness of the proposed control is highlighted by the fact that these improvements are achieved with both continuous and peak actuator limits as well as for different constant exogenous SL position commands. Additionally, the controllers designed for one corner of the car have also been tested in the full-car nonlinear model. The results obtained are promising and will serve as basic benchmarks for the design of full-car specific controllers.

Future work will focus on increasing the range of operating conditions for which a single controller provides good performance, on the application of gain-scheduling techniques (Fialho & Balas, 2002), on the co-design of the passive and active components of the suspension, on the synthesis of controllers for the full-car, and on model validation through experimental testing (Arana et al., 2015).

Also, the ability of the proposed control to follow different exogenous position commands, especially at low frequencies, may be utilized to blend this high frequency control with the body attitude control proposed in Arana et al. (2016). Finally, it is interesting to investigate the possible benefits of combining the SAVGS with a semi-active suspension strut rather than a passive one, against the obvious disadvantages of increased complexity.

Appendix A

Table A.4
Main vehicle and SAVGS parameters (F: front, R: rear).

Parameter	Units	Axle	Value
Total/Sprung mass	kg	–	1525/1325
Wheelbase/CM height	mm	–	2600/424
Weight distribution	%	F/R	43/57
Spring stiffness	N/mm	F/R	92/158
Tire stiffness	N/mm	F& R	275
Installation ratio	–	F/R	0.60/0.56
SL lengths	mm	F/R	15/11
Actuator mass	kg	F& R	6
Gear ratio	–	F& R	40
Peak output torque	Nm	F& R	205
Max. output speed	rpm	F& R	137

References

Anon., (1998). Autosim 2.5+ Reference Manual, Mechanical Simulation Corporation. 709 West Huron, Ann Arbor MI, ⟨http://www.carsim.com⟩.

Arana, C., Evangelou, S. A., & Dini, D., (2012). Pitch angle reduction for cars under acceleration and braking by active variable geometry suspension. In *2012 IEEE Proceedings of the 51st IEEE Conference on Decision and Control (CDC)*. pp. 4390–4395.

Arana, C., Evangelou, S. A., & Dini, D., (2014). Car attitude control by series mechatronic suspension. {*IFAC*} *Proceedings Volumes 47* (3) pp. 10688 – 10693, 19th {IFAC} World Congress.

Arana, C., Evangelou, S. A., & Dini, D. (2015). Series active variable geometry suspension for road vehicles. *IEEE/ASME Transactions on Mechatronics*, *20*(*1*), 361–372.

Arana, C., Evangelou, S. A., & Dini, D. (2016). Series active variable geometry suspension application to chassis attitude control. *IEEE/ASME Transactions on Mechatronics*, *21*(*1*), 518–530.

Basari, A. A., Sam, Y. M., Hamzah, N., (2007). Nonlinear active suspension system with backstepping control strategy. In *Proceedings of the 2nd IEEE Conference on Industrial Electronics and Applications*, pp. 554–558.

Beaven, R., Wright, M., & Seaward, D. (1996). Weighting function selection in the $\mathcal{H}_\infty$ design process. *Control Engineering Practice*, *4*(*5*), 625–633.

Bibel, J. E., & Malyevac, D. S., (1992). Guidelines for the selection of weighting functions for H-infinity control. Weapons Systems Department, Naval Surface Warfare Center, Dahlgren Division, Virginia, DTIC Document.

Cao, J., Liu, H., Li, P., & Brown, D. J. (2008). State of the art in vehicle active suspension adaptive control systems based on intelligent methodologies. *IEEE Transactions on Intelligent Transportation Systems*, *9*(*3*), 392–405.

Chen, P.-C., & Huang, A.-C. (2006). Adaptive sliding control of active suspension systems with uncertain hydraulic actuator dynamics. *Vehicle System Dynamics*, *44*(*5*), 357–368.

Chen, H., & Scherer, C. W., (2004). An LMI based model predictive control scheme with guaranteed $\mathcal{H}_\infty$ performance and its application to active suspension. In *American Control Conference. Proceedings of the, Vol. 2*, pp. 1487–1492.

Cheng, C., Evangelou, S. A., Arana, C., & Dini, D., (2015). Active variable geometry suspension robust control for improved vehicle ride comfort and road holding. In *2015 American Control Conference (ACC)*, pp. 3440–3446.

Do, A., Sename, O., Dugard, L., & Soualmi, B., (2011). Multi-objective optimization by genetic algorithms in $\mathcal{H}_\infty$/*LPV* control of semi-active suspension. *IFAC Proceedings Volumes 44* (1) (2011) pp. 7162–7167, 18th IFAC World Congress.

Doyle, J., Glover, K., Khargonekar, P., & Francis, B. (1989). State-space solutions to standard $\mathcal{H}_2$ and $\mathcal{H}_{infty}$ control problems. *IEEE Transactions on Automatic Control*, *34*(*8*), 831–847.

Doyle, J., Packard, A., & Zhou, K., (1991). Review of LFTs, LMIs, and μ. In *Proceedings of the 30th IEEE Conference on Decision and Control (CDC)*, pp. 1227–1232.

Evangelou, S. A., Dini, D., De Meerschman, O., Tocatlian, A., Kneip, C., & Palas, C., (2011). Variable-geometry suspension apparatus and vehicle comprising such apparatus. US Grant, 2010-08-26, July, US9026309B2.

Fergani, S., Sename, O., & Dugard, L. (2016). An LPV/$\mathcal{H}_\infty$ integrated vehicle dynamic controller. *IEEE Transactions on Vehicular Technology*, *65*(*4*), 1880–1889. http://dx.doi.org/10.1109/TVT.2015.2425299.

Fialho, I., & Balas, G. (2002). Road adaptive active suspension design using linear parameter-varying gain-scheduling. *IEEE Transactions on Control Systems Technology*, *10*(*1*), 43–54.

Gáspár, P., & Németh, B., Integrated control design for driver assistance systems based on lpv methods. *International Journal of Control 0* (0) (0) pp. 1–14. http://dx.doi.org/doi:10.1080/00207179.2016.1160292.

Gaspar, P., Szaszi, I., & Bokor, J. (2003). Design of robust controllers for active vehicle suspension using the mixed μ synthesis. *Vehicle System Dynamics*, *40*(*4*), 193–228.

Gillespie, T. D., (1992). Fundamentals of vehicle dynamics.

Glover, K., & Doyle, J. C. (1988). State-space formulae for all stabilizing controllers that satisfy an $\mathcal{H}_\infty$-norm bound and relations to risk sensitivity. *Systems & Control Letters*, *11*(*3*), 167–172.

Green, M., & Limebeer, D. (1995). *Linear robust control*. Prentice Hall.

Hedrick, J. K., & Butsuen, T. (1990). Invariant properties of automotive suspensions. *Proceedings of the Institution of Mechanical Engineers, Part D: Journal of Automobile Engineering*, *204*(*1*), 21–27.

ISO, 8608:1995, (1995). Mechanical vibration - Road surface profiles - reporting of measured data.

Karnopp, D. (1986). Theoretical limitations in active vehicle suspensions. *Vehicle System Dynamics*, *15*(*1*), 41–54.

Li, H., Yu, J., Hilton, C., & Liu, H. (2013). Adaptive sliding-mode control for nonlinear active suspension vehicle systems using t-s fuzzy approach. *IEEE Transactions on Industrial Electronics*, *60*(*8*), 3328–3338.

Lundström, P., Skogstad, S., & Wang, Z., (1991). Weight selection for H-infinity and mu-control methods - Insights and examples from process control. In *Symposium on Robust Control System Design Using H-infinity and Related Methods*, Cambridge, UK.

MarketsandMarkets. Automotive suspension systems market worth $66.2 billion by 2018,Accessed 22.12.14. [Online] ⟨http://www.marketsandmarkets.com/PressReleases/automobile-suspension-systems.asp⟩.

Safonov, M. G., Limebeer, D. J. N., & Chiang, R. Y. (1989). Simplifying the $\mathcal{H}_\infty$ theory via loop-shifting, matrix-pencil and descriptor concepts. *International Journal of Control*, *50*(*6*), 2467–2488.

Sammier, D., Sename, O., & Dugard, L. (2003). Skyhook and h-infinity control of semi-active suspensions: some practical aspects. *Vehicle System Dynamics*, *39*(*4*), 279–308.

Savaresi, S. M., Poussot-Vassal, C., Spelta, C., Sename, O., & Dugard, L. (2010). *Semi-active suspension control design for vehicles*. Elsevier.

Sharp, R. S., & Bettella, M. (2003). Shear force and moment descriptions by normalisation of parameters and the magic formula. *Vehicle System Dynamics*, *39*(*1*), 27–56.

Sharp, R. S., & Crolla, D. A. (1987). Road vehicle suspension system design - a review. *Vehicle System Dynamics*, *16*(*3*), 167–192.

Sharp, R. S., & Peng, H. (2011). Vehicle dynamics applications of optimal control theory. *Vehicle System Dynamics*, *49*(*7*), 1073–1111.

Sharp, R. S. (1998). Variable geometry active suspension for cars. *Computing Control Engineering Journal*, *9*(*5*), 217–222.

Sharp, R. S. (2004). Testing and improving a tyre shear force computation algorithm. *Vehicle System Dynamics*, *41*(*3*), 223–247.

Smith, M. C., & Walker, G. W. (2000). Performance limitations and constraints for active and passive suspensions: a mechanical multi-port approach. *Vehicle System Dynamics*, *33*(*3*), 137–168.

Smith, M. C. (1995). Achievable dynamic response for automotive active suspensions. *Vehicle System Dynamics*, *24*(*1*), 1–33.

Türkay, S., & Akçay, H. (2008). Aspects of achievable performance for quarter-car active suspensions. *Journal of Sound and Vibration*, *311*(*1–2*), 440–460.

Tseng, H. E., & Hrovat, D. (2015). State of the art survey: active and semi-active suspension control. *Vehicle System Dynamics*, *53*(*7*), 1034–1062.

Van De Wal, M., Philips, P., & De Jager, B. (1998). Actuator and sensor selection for an

active vehicle suspension aimed at robust performance. *International Journal of Control*, *70*(*5*), 703–720.
van der Sande, T., Gysen, B., Besselink, I., Paulides, J., Lomonova, E., & Nijmeijer, H. (2013). Robust control of an electromagnetic active suspension system: Simulations and measurements. *Mechatronics*, *23*(*2*), 204–212.
van der Sande, T., Gysen, B., Besselink, I., Paulides, J., Lomonova, E., & Nijmeijer, H. (2013). Robust control of an electromagnetic active suspension system: simulations and measurements. *Mechatronics*, *23*(*2*), 204–212 (special Issue on Linear DrivesDrives).
Yue, C., Butsuen, T., & Hedrick, J. K., (1988). Alternative control laws for automotive active suspensions. In *American Control Conference (ACC)*, pp. 2373–2378.
Zhou, K., & Doyle, J. (1998). *Essentials of robust control*. Prentice Hall.
Zin, A., Sename, O., Gaspar, P., Dugard, L., & Bokor, J. (2008). Robust LPV-$\mathcal{H}_\infty$ control for active suspensions with performance adaptation in view of global chassis control. *Vehicle System Dynamics*, *46*(*10*), 889–912.